J. Fluid Mech. (2009), *vol.* 633, *pp.* 17–60.
doi:10.1017/S0022112009006934 Printed in the United Kingdom

Buffer layer structures associated with extreme wall stress events in a smooth wall turbulent boundary layer

J. SHENG†, E. MALKIEL AND J. KATZ†‡

Department of Mechanical Engineering, The Johns Hopkins University, Baltimore MD 21218, USA

(Received 20 October 2008 and in revised form 28 February 2009)

Three-dimensional velocity distributions and corresponding wall stresses are measured concurrently in the inner part of a turbulent boundary layer over a smooth wall using digital holographic microscopy. The measurements are performed in a square duct channel flow at $Re_\delta = 50\,000$ and $Re_\tau = 1470$. A spatial resolution of 3–8 wall units ($\delta_\upsilon = 17\,\mu$m) in streamwise and spanwise directions and 1 wall unit in the wall-normal direction are sufficient for resolving buffer layer structures and for measuring the instantaneous wall shear stresses from velocity gradients in the viscous sublayer. Mean velocity and Reynolds stress profiles agree well with previous publications. Rudimentary observations classify the buffer layer three-dimensional flow into (i) a pair of counter-rotating inclined vortices, (ii) multiple streamwise vortices, some of them powerful, and (iii) no apparent buffer layer structures. Each appears in about one third of the realizations. Conditional sampling based on local wall shear stress maxima and minima reveals two types of three-dimensional buffer layer structures that generate extreme stress events. The first structure develops as spanwise vorticity lifts from the wall abruptly and within a short distance of about 10 wall units, creating initially a vertical arch. Its only precursors are a slight velocity deficit that does not involve an inflection point and low levels of vertical vorticity. This arch is subsequently stretched vertically and in the streamwise direction, culminating in formation of a pair of inclined, counter-rotating vortices with similar strength and inclination angle exceeding 45°. A wall stress minimum exists under the point of initial lifting. A pair of stress maxima develops $35\delta_\upsilon$ downstream, on the outer (downflow) sides of the vortex pair and is displaced laterally by 35–$40\delta_\upsilon$ from the minimum. This flow structure exists not only in the conditionally averaged field but in the instantaneous measurement as well and appears in 16.4 % of the realizations. Most of the streamwise velocity deficit generated by this phenomenon develops during this initial lifting, but it persists between the pair of vortices. Distribution of velocity fluctuations shows that spanwise transport of streamwise momentum plays a dominant role and that vertical transport is small under the vortices. In other regions, e.g. during initial lifting, and between the vortices, vertical transport dominates. The characteristics of this structure are compared to early experimental findings, highlighting similarities and differences. Abundance of pairs of streamwise vortices with similar strength is inconsistent with conclusions of several studies based on analysis of direct numerical simulation (DNS) data. The second buffer layer structure generating high wall stresses is a single, predominantly streamwise vortex, with characteristic diameter of 20–$40\delta_\upsilon$

† Present address: Aerospace Engineering and Mechanics, University of Minnesota, Minneapolis MN 55455, USA.

‡ Email address for correspondence: katz@jhu.edu

and inclination angle of 12°. It generates an elongated, strong stress maximum on one side and a weak minimum on the other and has been observed in 20.4 % of the realizations. Except for a limited region of sweep above the high-stress region, this low-lying vortex mostly induces spanwise momentum transport. This structure appears to be similar to those observed in several numerical studies.

1. Introduction

Generation and advection of turbulent flow structures in the inner parts of turbulent boundary layers over smooth walls and their impact on turbulence production and wall shear stresses have been studied for many decades. Despite considerable progress and vast literature, progress has not been commensurate with efforts, reflecting the flow complexity and technical difficulties in characterizing it. These studies have established that part of the boundary layer turbulence consists of quasi-periodic coherent motions, which are apparently major contributors to turbulence production, dissipation and transport. Although large-scale eddies in the outer layer contain a substantial fraction of the overall energy, nearly all of the turbulent kinetic energy (TKE) production in a boundary layer occurs in the near-wall region (Klebanoff 1954; Pope 2000). The associated high Reynolds shear stress implies high inter-correlation between two velocity fluctuation components, which is most likely a result of organized motions in the viscous sublayer and buffer regions. Their importance to our understanding of boundary layer dynamics motivates us to focus in this paper on buffer layer flow structures and examine the relationship between fluctuating wall shear stress and the passage of coherent motions in the near-wall region.

Past research has generated a vast number of publications on coherent motion in turbulent boundary layers, too many to summarize in a single paper. Here we only summarize the prevailing findings, conjectures and open questions, which are relevant to the current work. In the sublayer and buffer regions, the streamwise velocity field is organized into persistent alternating narrow streaks of high-speed and relatively quiescent low-speed flows. The majority of TKE production occurs in the buffer region during intermittent, violent outward ejections of low-speed fluid and during inrushes of high-speed fluid at a shallow angle towards the wall. The ejections are considered to be an intermittent, quasi-cyclic process and are often referred to as 'bursting', a subject of numerous experimental (Klebanoff, TrDsTRom & Sargent 1962; Kline *et al.* 1967; Smith & Metzler 1983; Acarlar & Smith 1987; Bech *et al.* 1995; see also the review in Robinson 1991) and computational studies (Hamilton, Kim & Waleffe 1995; Holmes, Lumley & Berkooz 1996; Itano & Toh 2001, 2005; Kawahara & Kida 2001; Schoppa & Hussain 2002; Jimenez *et al.* 2005; Viswanath 2007). The mechanisms that have been proposed to explain the origin and dynamics of bursting (Hamilton *et al.* 1995; Holmes *et al.* 1996; Itano & Toh 2001, 2005; Kawahara & Kida 2001; Schoppa & Hussain 2002) can be divided into two groups: (i) Those consisting of intermittent eruption of fluid away from the wall due to some form of local instability (Suponitsky, Cohen & Bar-Yoseph 2005) and (ii) those involving ejection of fluid away from the wall caused by passage of one or more tilted, quasi-streamwise vortices, which persist for considerably long periods of time (Acarlar & Smith 1987; Clark & Markland 1971; Jimenez & Pinelli 1999; Kim, Kline & Reynolds 1971; Nakagawa & Nezu 1981). Both involve vortical structures, the former in the form of inner layer disturbance growth to form vortices under the influence of outer layer flow structures, with the latter occurring due to

passage of inner layer vortical structures. These mechanisms differ in temporal scales and whether flow instability is involved. Recent studies by Hamilton *et al.* (1995), Waleffe (1997), Kawahara & Kida (2001) and Viswanath (2007) suggest that quasi-periodic bursting can be elucidated by periodic solutions to the Navier–Stokes equation under proper boundary conditions. Still, in spite of these efforts there is no consensus on the answers to the following questions: (i) What is bursting? (ii) What types of structures are directly responsible for its occurrence? (iii) What is the role of bursting in generation, growth and suppression of near-wall flow structures? In this paper, it is not our objective or within our ability to answer these questions completely. However, we do provide direct, fully resolved, three-dimensional measured data showing quantitatively the characteristics of bursting-like events associated with extreme wall shear stresses and the near-wall flow structures generating them. We also elucidate their impact on the distributions of associated Reynolds and wall shear stresses (§ 3.4).

A second extensively debated topic involves characteristics of vortical structures within the inner portion of a turbulent boundary layer and their relationship with fluctuating quantities near the wall as well as structures located in outer parts of the boundary layer. Due to the limitation of available experimental and computational techniques, such as direct numerical simulation (DNS; e.g. Kim, Moin & Moser 1987) and planar particle image velocimetry (PIV; e.g. Adrian 1991; Ganapathisubramani, Longmire & Marusic 2003; Hutchins, Hambleton & Marusic 2005), the vast majority of our knowledge of near-wall turbulent structures has been obtained from computations at low Reynolds number ($Re_\theta < 5000$) and/or experiments involving limited spatio-temporal dimensions. A number of different shapes and topologies have been proposed for near-wall ($y^+ < 100$) vortices. Quasi-streamwise, outward-tilted vortices that are visible in the x–z plane (with x and z the streamwise and spanwise coordinates, respectively) have been observed in flow visualizations by Smith & Schwartz (1983) and Kasagi, Hirata & Nishino (1986), as well as by inclined PIV measurement by Hutchins *et al.* (2005). Transverse vortices have been observed in convecting and stationary x–y views (Clark & Markland 1971; Praturi & Brodkey 1978; Smith & Lu 1989; Adrian, Meinhart & Tomkins 2000; Liu, Adrian & Hanratty 2001; Wu & Christensen 2006). Extension of the legs of these vortices into the upper buffer layer has been seen in inclined dual-plane PIV measurements (Ganapathisubramani *et al.* 2003, 2005; Hutchins *et al.* 2005), and their impact on the wall shear stress was determined based on correlations between the stress and streamwise velocity (Marusic & Heuer 2007). Due to the complexity and three-dimensionality of near-wall flow structures, direct observations on topology and spatial scale have been made by qualitative flow visualizations at low Reynolds numbers (Willmarth & Woolridge 1962; Kline *et al.* 1967; Corino & Brodkey 1969; Clark & Markland 1971; Often& Kline 1974; Offen & Kline 1975; Klewicki & Hirschi 2004) or via numerical simulations (e.g. Kim *et al.* 1987; Jimenez 1999; Jimenez & Pinelli 1999; Zhou *et al.* 1999; Jimenez 2000; Jimenez, Del Alamo & Flores 2004; Jimenez *et al.* 2005). Quantitative descriptions based on experimental measurements have been inferred via conditional sampling (e.g. Wallace, Eckelmann & Brodkey 1972; Willmarth & Lu 1972) or deduced via inspection of projected two-dimensional signatures of passing structures (e.g. Adrian *et al.* 2000; Ganapathisubramani *et al.* 2003; Hutchins *et al.* 2005). These studies have shown that near-wall flow turbulence is greatly influenced by passage of streamwise vortical structures, but debates on their origin and relationship with structures located in outer parts of the boundary layer have remained unsettled. Differences are often found in what are perceived as the

dominant near-wall flow structures, as well as their relationships with the (elusive) bursting phenomenon, formation of low-speed streaks and the low wall shear stress beneath them. In the present paper we focus on near-wall structures generating high and low extreme wall stress events.

The discussion on boundary layer structures was initiated by Theodorsen (1952) who proposed a hairpin vortex model with spanwise symmetry and two quasi-streamwise legs inclined at 45°. The spanwise dimensions of these instantaneous structures were proportional to the distance from the wall. Willmarth & Tu (1967) used space–time correlation between local wall pressure and velocity components to devise an ensemble model depicting vorticity lines sloped downstream at about 10° from the wall. They did emphasize that this model only portrayed an average structure, which did not exist in the instantaneous fields. Willmarth & Lu (1972) further suggested that near-wall hairpin vortices might evolve to larger-scale, outer layer structures, which were responsible for creating characteristic bulges at the edge of a turbulent boundary layer. Kline, *et al.* (1967), Kim *et al.* (1971) and Offen & Kline (1974, 1975) described a model featuring a lifted and stretched horseshoe-shaped vortex loop, which appeared consistent with the conjecture that passage of a horseshoe vortex was linked with the near-wall bursting process. Hinze (1975) proposed a model relating many observed near-wall turbulence production features to the dynamics of horseshoe-shaped vortices. These vortices were initiated from spanwise vortices and then lifted and stretched to form two quasi-streamwise counter-rotating vortices as legs. Head & Bandyopadhyay (1981) used smoke flow visualization to show hairpin-shaped structures dominating the boundary layer over a range of Reynolds number. With elongated trailing legs and with a head inclination angle of 45° with the wall, these hairpin vortices were often large and resided in the outer layer. Wallace (1982) summarized previous results and conjectured that hairpin vortices originating from kinks in spanwise vortex line were the dominant near-wall flow structures.

Smith (1984) and Acarlar & Smith (1987), drawing conclusions from kernel experiments involving injection from the wall into laminar boundary layers, proposed a rather complete conceptual model for hairpin vortices in the wall region. This model described both the kinematics and the dynamics of these hairpins and their relations with low-speed streaks, bursting, near-wall shear layers, ejections and sweeps. The vortices were formed in the unstable shear layer located on the top and sides of the tap and, once formed, moved away from the wall by self-induction. The trailing legs remained in the near-wall region but were stretched, forming counter-rotating quasi-streamwise vortices that pumped fluid away from the wall and accumulated low-speed fluids between the legs. They speculated that coalescence of the stretched legs of multiple hairpin packets was the mechanism maintaining the low-speed streaks. Formation of hairpin vortices from the unstable shear layer was attributed to the production cycle of bursting events. Adrian & Moin (1988), using stochastic estimation of DNS results for channel flow, also showed hairpin-shaped vortices with two streamwise legs but emphasized that their structure was only a statistical model. Zhou *et al.* (1999), using DNS based on a disturbance extracted from PIV data (Adrian *et al.* 2000), demonstrated a regeneration mechanism of hairpin-shaped vortex developing into a packet of vortices. They suggested that the hairpin packets were the dominant flow structures in the outer region of a turbulent boundary layer. Hutchins *et al.* (2005) and Ganapathisubramani *et al.* (2003, 2005) used various PIV techniques to investigate the outer layer dynamics and showed that hairpin vortices inclined at 45° to the wall appeared at $y^+ = 25$. We will return to these theories after introducing the present data on three-dimensional buffer layer structures.

Different pictures have been drawn based on statistical analysis of DNS data. For example, Perry & Chong (1986) and Perry, Henbest & Chong (1986) extended Perry & Chong's (1982) model consisting of a forest of Λ-shaped vortices. Walker & Herzog (1988) and Hanratty (1989) proposed hairpin-like models capturing key aspects of the quasi-streamwise vortex structures in the buffer and lower log layers. Bakewell & Lumley (1967), Herzog (1986) and Aubry *et al.* (1988) utilized proper orthogonal decomposition to identify near-wall coherent motions, e.g. array of counter-rotating pairs of streamwise vortices, and demonstrated that such coherent motions would generate burst-like dynamics. Kim (2003) examined structures in DNS data and claimed that most of the vortices in the log layer appeared as singles, not as pairs. Even when conditional averaging of DNS data showed a pair of counter-rotating streamwise vortices, e.g. in the vicinity of wall shear stress maximum (Kravchenco *et al.* 1993), they were not found in instantaneous data. Instead, local stress fluctuations were more often than not caused by single quasi-streamwise vortices, not by pairs. Jeong & Hussain (1995), Jeong *et al.* (1997) and subsequently Schoppa & Hussain (2000, 2002) proposed a model consisting of staggered single streamwise vortices with opposite vorticity and showed, using conditional sampling based on alignment, that such a spatial arrangement reproduced the wall stress distributions and turbulence statistics, including occurrence of bursts. Recent papers by Jimenez and colleagues (Jimenez 1999, 2000; Jimenez & Pinelli 1999; Jimenez *et al.* 2004, 2005) also concluded that the flow dynamics in the inner part of a boundary layer were dominated by isolated streamwise vortices and not by hairpin structures or by pairs of vortices with similar circulation. Jimenez & Pinelli (1999) showed that low-speed streaks associated with streamwise vortices persisted for a long distance and were occasionally disrupted by bursts, which involved lifting of a vortex section away from the wall, immediately followed by another similar structure.

In summary, although there is a consensus that near-wall streamwise vortices with low inclination angles exist and play dominant roles, there is no agreement about their origin and relationship with other neighbouring structures. In an attempt to elucidate this issue, in this paper, we apply a recently developed technique, in-line digital holographic microscopy (DHM; Sheng *et al.* 2007*a*, 2007*b*; Sheng, Malkiel & Katz 2008), to simultaneously measure, for the first time, both components of the instantaneous wall shear stress and three-dimensional velocity distribution in the $0 < y^+ < 100$ range. The measurement resolution is equivalent to current DNS, about 3 wall units in the streamwise and spanwise directions and 1 wall unit in the wall-normal direction. This unique experimental database on three-dimensional buffer layer flow structures and associated wall shear stresses in a high-Reynolds-number boundary layer enables us to examine some of the aforementioned conceptual models. We use it to identify and quantify two distinctly different types of buffer layer structures that generate extreme wall stresses. First, we show conclusively that lifted spanwise vorticity forming a pair of quasi-streamwise vortices, in agreement with classical flow concepts, plays a significant role in generating both wall stress minima and wall stress maxima. This phenomenon exists both in instantaneous and conditionally averaged data; i.e. it is not an artefact of averaging. The mechanisms involved as well as the size, shape, alignment and impact of this structure on formation of low-speed streaks and Reynolds stresses are also quantified. Second, we find that low-lying, single buffer layer vortices also contribute substantially to generation of stress maxima and to a lesser extent to formation of stress minima and low-speed streaks. This type of structures appears to be consistent with several of the above-mentioned observations based on DNS data. We characterize the shape

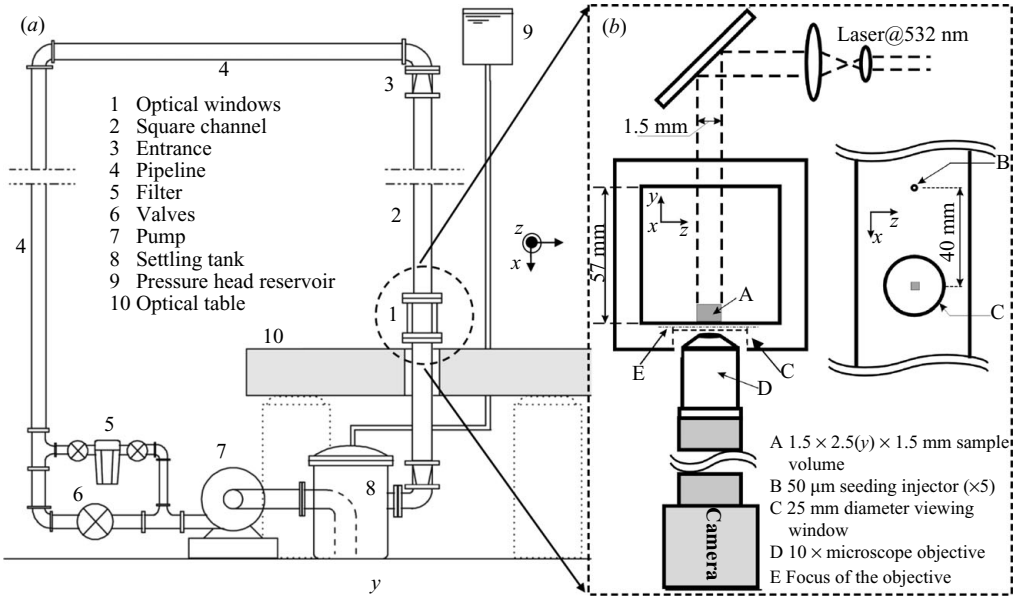

FIGURE 1. Test facility and DHM set-up.

and alignment of this structure, as well as its impact on distribution of Reynolds stresses.

Brief descriptions of the experimental set-up, measurement technique, accuracy and procedures are provided in § 2. Data on mean and fluctuating flow parameters are provided in § 3.1, followed by a brief description and tabulation of characteristic flow structures and wall stress distributions in § 3.2. Results of conditional sampling of flow and stresses based on local stress minima and maxima are presented in § 4. A detailed discussion and comparisons of previous studies are summarized in § 5.

2. Facility and methodology

2.1. *Facility, measurement and uncertainties*

Details of the facility and measurement methodology of the present study can be found in Sheng *et al.* (2008) and are only described briefly here. As illustrated in figure 1, measurements are performed in a vertical 57 mm × 57 mm square-duct water facility (Zhang, Tao & Katz 1997; Tao, Katz & Meneveau 2000, 2002), and the sample volume is situated at 3.3 m (∼60 diameters) downstream of a honeycombed entrance. The measurement volume has dimensions of 1.5 mm × 2.5 mm × 1.5 mm in the streamwise, wall-normal and spanwise directions, denoted as x, y and z respectively, which is equivalent to 88 × 145 × 88 wall units, as justified below. The corresponding velocity components are u, v and w. The sample volume is locally seeded with 2 μm monodispersed polystyrene particles. To prevent the seeding process from disturbing the local turbulent boundary layer, the particles are injected by a motorized syringe through a set of five 50 μm injectors located 40 mm (∼800 injector diameters) upstream of the sample volume. The mean exit velocity is 2 mm s^{-1}, i.e. 0.1 % of the centre line velocity $U_c = 2$ m s^{-1}. At this velocity ratio, the fluid containing the particles is expected to remain close to the wall (Gopalan, Abraham & Matz 2004), as confirmed by the present particle penetration depth of less than 2 mm about 75 mm downstream

of the injectors. To prevent adverse effects of surface discontinuities, the inner surface of the wall is kept intact in the vicinity of the sample volume; i.e. the bore containing the microscope objective does not penetrate into the inner wall.

In-line DHM (Sheng, Malkiel & Katz 2006; Sheng *et al.* 2007*a*, 2008) is used for recording the three-dimensional location of particle in the sample volume using the optical set-up illustrated in figure 1. Numerical reconstruction and three-dimensional segmentation are then used for determining the location of each particle. Then, particle tracking velocimetry (PTV) is applied to measure the velocity of each particle from the displacement in successive frames. The number of vectors in individual realizations varies from 2000 to 10 000 with a mean nearest neighbour distance of 50–100 μm, i.e. 3–8 wall units (provided in § 3.1). However, the particles are mostly concentrated near the wall, where they provide an averaged mean nearest neighbour distance in the wall-normal direction of less than 15 μm (<1 wall unit) and in the streamwise and spanwise directions of about 3 wall units. During interpolation on to a regular grid, we use the nearest 30 velocity measurements that are located within a search ellipsoid that has long axes of 5 wall units aligned parallel to the wall (∼85 μm) and a short axis of 2.5 wall units (∼45 μm) perpendicular to the wall. We also account for velocity gradients using first-order Taylor expansion. Details on the acquisition, reconstruction, segmentation, procedures and algorithms associated with particle tacking as well as interpolation on to a regular grid are provided in Sheng *et al.* (2008).

Our analysis and previous experiments (Sheng *et al.* 2006) have shown that DHM allows us to locate particles in a three-dimensional space with an accuracy of approximately 2–3 particles diameter in the beam axis direction (y) and about 0.4 diameter in directions perpendicular to this axis. To estimate the accuracy of our velocity measurements, we calculate the probability distributions of the normalized velocity divergence,

$$\sigma = \left(\frac{\partial u}{\partial x} + \frac{\partial v}{\partial y} + \frac{\partial w}{\partial z}\right)^2 \Bigg/ \left[\left(\frac{\partial u}{\partial x}\right)^2 + \left(\frac{\partial v}{\partial y}\right)^2 + \left(\frac{\partial w}{\partial z}\right)^2\right], \tag{2.1}$$

over the first 100 realizations. The average value of σ varies between 0, if the velocity distribution is divergence-free, and 1 for random data (Zhang *et al.* 1997). Figure 2 (Sheng *et al.* 2008) compares the present probability density function (p.d.f.) and cumulative distribution of σ to those of our previous three-dimensional holographic velocity measurements, obtained using two perpendicular views and complex off-axis optical set-up (Zhang *et al.* 1997; Sheng, Malkiel & Katz 2003). Clearly, the present results are substantially more divergence-free than previous data. To quantify the error in the wall-normal direction, which is the least accurate, we add random errors with standard deviation, denoted as ε, to our measured wall-normal component and re-evaluate the normalized divergence. As is evident, the divergence-free condition deteriorates very quickly when ε is increased from 1.25 mm s^{-1} to 2.5 mm s^{-1}. Figure 2 suggests that our measurements have uncertainties that are better than 1.25 mm s^{-1} in all directions, i.e. less than 0.1 % of the free-stream velocity.

Instantaneous wall shear stresses $\tau_{xy} = \mu \partial u/\partial y|_{y=0}$ and $\tau_{zy} = \mu \partial w/\partial y|_{y=0}$ are estimated from the slope of local velocity profiles in the viscous sublayer, i.e. $y \leqslant 75$ μm or $y^+ \leqslant 4.5$. To determine this slope, we divide the viscous sublayer into sub-volumes of 150 μm × 75 μm × 150 μm and apply linear regression over all velocity vectors measured within each volume. A sample is presented in figure 2(b). Thus, the spatial resolution of skin friction presented here is 150 μm, about 9 wall units. The standard

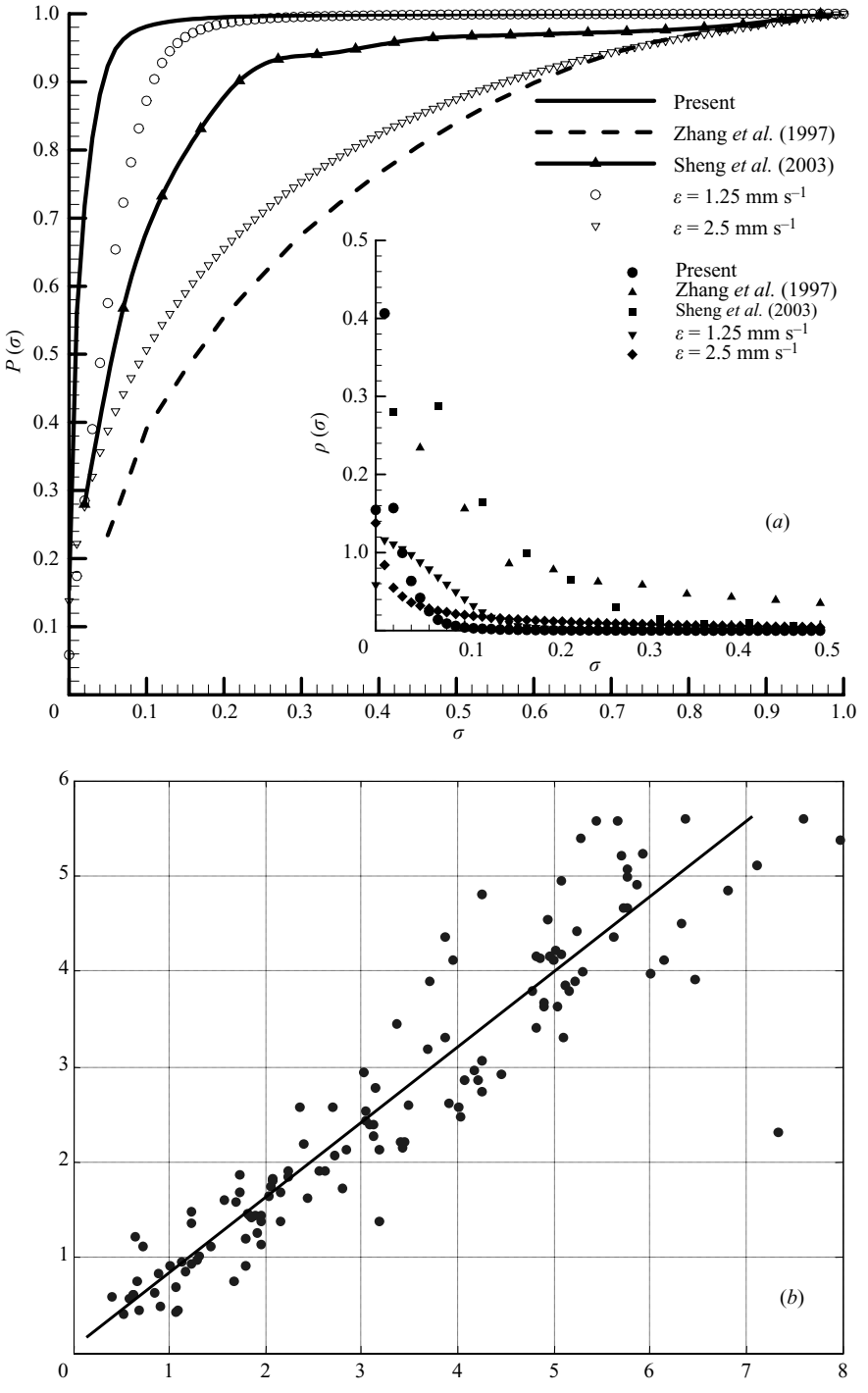

FIGURE 2. (*a*) Cumulative probability distribution of the present normalized divergence, σ (2.1), in comparison with those obtained in previous measurements and when we artificially introduce random errors with standard deviation of ε. The insert is the corresponding p.d.f. (*b*) Illustration of method for measuring the local wall shear stress using linear regression of velocity within a 150 μm × 75 μm × 150 μm volume in the viscous sublayer.

deviation of scatter around regression lines is ~8 %. This uncertainty is well below measured spatial variations in stress of 60–300 % and hence has minor consequence in interpretation of results.

2.2. *Conditional sampling*

To identify causal relationship between wall stress events and buffer layer structures, we rely on the conditional-averaging technique introduced in Antonia (1981) and subsequently applied by Kim *et al.* (1987) to channel flow and by Adrian & Moin (1988) to homogeneous shear flow. Another possible approach to elucidate dominant buffer layer structures is the characteristic-eddy method (Bakewell & Lumley 1967; Lumley 1983). However, since our intention is to associate two co-occurring phenomena, i.e. near-wall flow structures and extreme wall shear stress events, conditional averaging based on the latter appears to be more suitable. We condition on local maxima and minima of streamwise wall shear stress τ_{xy}, following the averaging procedure detailed in Kim *et al.* (1987). When the wall shear stress maximum exceeds a certain threshold, the sampling procedure is

$$\hat{V}^{max}(\Delta x, y, \Delta z) = \langle V(x - x_m, y, z - z_m) | \tau_{xy}(x_m, z_m) > \alpha \langle \tau_{xy} \rangle \text{ and } \max(\tau_{xy}) = \tau_{xy}(x_m, z_m) \rangle, \quad (2.2)$$

where $\langle\,\rangle$ denote ensemble averaging; hat refers to conditional (and shifted) sampling, $\Delta x = x - x_m$; V represents any variables including three-dimensional velocity distribution, (u, v, w), and its derivatives, $\partial_i u_j$, or invariants of the velocity gradient tensor; and α is a fraction greater than 1. Equation (2.2) describes an alignment procedure that translates the three-dimensional fields laterally such that the local maximum is relocated to the origin of the averaged field. For conditional averaging based on the local stress minimum events below a certain threshold, the procedure is defined as

$$\hat{V}^{min}(\Delta x, y, \Delta z) = \langle V(x - x_m, y, z - z_m) | \tau_{xy}(x_m, z_m) < \beta \langle \tau_{xy} \rangle \text{ and } \min(\tau_{xy}) = \tau_{xy}(x_m, z_m) \rangle, \quad (2.3)$$

where β is a coefficient less than 1. Since multiple points in the same instantaneous distribution may satisfy the same condition, including all of these points in the averaging, as done in Kim *et al.* (1987) and Kravechenko *et al.* (1993), the flow feature of interest in both the spanwise and streamwise directions tends to get smeared. Consequently, we include an instantaneous flow field satisfying the condition only once in the averaging procedure and locate the local maximum and minimum points at the origin of the conditionally sampled fields.

3. Velocity, Reynolds stresses and characterization of structures

3.1. *Mean flow and turbulence statistics*

Summarizing relevant data presented in Sheng *et al.* (2008), mean and fluctuating velocity distributions are computed over 750 instantaneous three-dimensional velocity distributions. The profile of mean streamwise velocity (figure 3*a*) displays the characteristic law of the wall for the inner layer of a smooth wall turbulent boundary layer (Pope 2000). The viscous sublayer, buffer layer and lower portion of logarithmic layer seem to be adequately resolved. We estimate the mean wall unit by linear

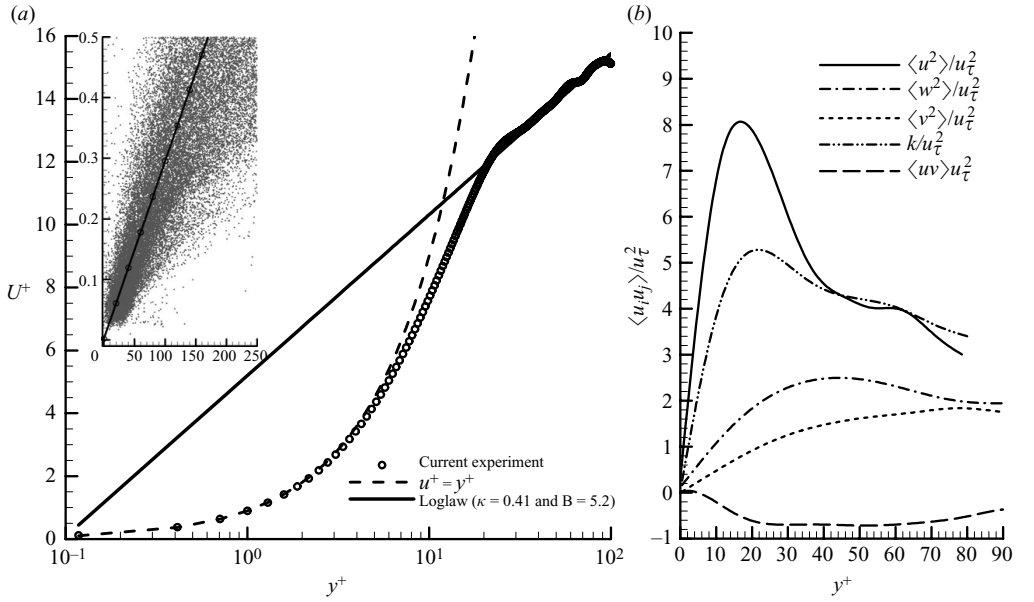

FIGURE 3. (*a*) Measured mean streamwise velocity profile obtained from 750 realizations compared to the law of the wall. Insert: data points and linear regression used for calculating u_τ. (*b*) Profiles of $\langle u^2\rangle$, $\langle v^2\rangle$, $\langle w^2\rangle$, $\langle k\rangle$ and $\langle uv\rangle$ normalized by u_τ^2.

regression using all the horizontal velocity data within the viscous sublayer, as illustrated in figure 3. The mean streamwise wall shear stress $\langle\tau_{xy}\rangle|_{y=0}$ ($y = 0$ will be omitted for brevity) is 3.19 N m^{-1}; i.e. the friction velocity $u_\tau = \sqrt{\tau_{xy}/\rho}$ is 56.5 mm s^{-1}, and the wall unit $\delta_\upsilon = \nu/u_\tau$ is 17 µm. The associated uncertainty based on the standard deviation of instantaneous data scatter is 4 %. As figure 3(*a*) confirms, a normalized velocity profile using this value matches the 'law of the wall' very well. The friction Reynolds number $Re_\tau = u_\tau\delta/\nu$, where δ is half-channel height, is 1470, and the outer variables' Reynolds number $Re_\delta = U_c\delta/\nu$, where U_c=2 m s^{-1} is the mean velocity in the channel, is 50 000.

Distributions of Reynolds stresses and TKE (figure 3*b*) show the expected near-wall distributions, e.g. formation of a constant shear stress layer in the $25 < y^+ < 60$ domain, and peaking of $\langle u'u'\rangle$ close to the wall. These trends agree with results of DNS of two-dimensional channel flows (Kim *et al.* 1987; Jimenez & Hoyas 2008) and with many other experimental measurements (e.g. Kline *et al.* 1967). The present values of $\langle u_i'u_j'\rangle/k$ (k is TKE) at the point of maximum TKE production ($\approx -\langle u_i'u_j'\rangle\partial\langle u\rangle/\partial y$) are compared to the DNS statistics in table 1. As is evident, there are only small differences between locations of peak production and magnitudes of stresses. The small discrepancies may be associated with differences in Reynolds number or geometry, e.g. weak secondary flows that occur in square ducts (Kawahara, Kline & Reynolds 1998; Kobayashi 2008). Clearly, trends of the mean flow and second-order moments in the inner part of the boundary layer in the current square duct are consistent with those of typical two-dimensional smooth wall turbulent boundary layers. In other words, the buffer layer structures, which are discussed later in this paper, produce typical first- and second-order statistics. Before concluding, note that the low magnitudes of $\langle v'v'\rangle/k$ in table 1 are a result of comparing data for a point located very near the wall, where Kim *et al.* (1987) provided specific values.

	Present experiment $Re = 50\,000$, $Re_\tau = 1470$	Two-dimensional Channel DNS $Re = 13\,750$	Channel DNS $Re_\tau = 2000$
y^+ of production peak	10.5	11.8	11.17
$\langle u'^2\rangle/k$	1.614	1.70	1.65
$\langle v^2\rangle/k$	0.056	0.04	0.038
$\langle w^2\rangle/k$	0.2823	0.26	0.31
$\langle uv\rangle/k$	−0.1516	−0.116	−0.1019

TABLE 1. The present turbulence statistics at y^+ of TKE production peak compared to results of channel DNS simulations by Kim *et al.* (1987) and Jimenez & Hoyas (2008).

Also, the undulations in the distribution of $\langle u'u'\rangle$ at large y^+ are most likely a result of insufficient data for convergence.

In many experimental studies that do not involve direct measurement of wall shear stress, the friction velocity has been estimated using several approaches. For example, wall stress has been estimated based on the Reynolds shear stress in the constant stress region, i.e. $u_\tau^R \sim \sqrt{-\langle u'v'\rangle_{max}/\rho}$ (Tennekes & Lumley 1972; Niederschulte, Adrian & Hanratty 1990; Djenidi & Antonia 1993,). For the present data, $-\langle u'v'\rangle_{max}/\rho u_\tau^2 \approx 0.7$, and the associated wall unit is $\delta_\upsilon^R = \nu/u_\tau^R = 14.1\,\mu$m. Another approach is based on a curve fit to the mean velocity profile in the log layer and using the law of the wall ($\kappa = 0.38$, $B = 0.54$), the so-called Clauser chart method (Clauser 1956; Bradshaw & Huang 1995; George & Castillo 1997; Wei, Schmidt & McMurtry 2005). Fitting a line to the log-layer part of our velocity profile (not shown), we obtain a length scale of $\delta_\upsilon^{CCM} = 12.9\,\mu$m. This estimate is consistent with that of Tao *et al.* (2002) based on mean velocity profiles obtained in the same facilities. We opt to use δ_υ, which is based on the measured wall stress, as the characteristic length scale for the rest of this paper. However, this choice impacts the normalized dimensions of buffer layer flow features, as discussed later.

3.2. *Rudimentary classification of buffer layer structures and their imprints on wall shear stresses*

In this section, we summarize our attempts to classify characteristic buffer layer structures and comment on their effects on the distributions of wall shear stresses. The conclusions are based on examination of 250 instantaneous realizations (as opposed to 100 in Sheng *et al.* 2008), and one should keep in mind that classifying structures is a subjective process. Our characterization of near-wall coherent structures is based on examination of vorticity and velocity distributions in selected y–z and x–y planes dissecting the sample volumes, by examining the shape of vortex lines, as well as by visualizing the three-dimensional structures using isosurfaces of λ_2 (the second eigenvalue of $S^2 + \Omega^2$, S_{ij} and Ω_{ij} being the symmetric and antisymmetric parts of the velocity gradient tensor, repectively; Jeong & Hussain 1995) and swirling strength (Adrian *et al.* 2000). We have found that three-dimensional plots of the latter two quantities capture similar 'large-scale' flow features, so only the λ_2 isosurfaces are presented. To make sure that our choice of λ_2 level does not affect our classification, we have examined the same flow at different levels. The appropriate level is selected to best illustrate our point, and we do not use λ_2 for quantitative conclusions. As summarized in table 2, we have identified the below-given types of flow features.

Flow structure	Occurrence (total 250)	Characteristics	Location	Size (d^+)	Peak vorticity ($\|\omega^+\|$)
Counter-rotating vortex pair generating anti-splatting flow between them.	41 (16 %)	(i) Ejection between two equal strength vortices (ii) Streamwise alignment 45° (iii) Spanwise spacing: $30\delta_v$–$40\delta_v$ (iv) $\tau_{xy} = 0.4$–0.8 (v) $d\tau_{yz}/dz < 0$	$y+ \in (0, 40)$ $\langle y^+ \rangle = 20$	10–20	>900
Pair of vortices generating splatting pattern	28 (11 %)	(i) Sweeping between two vortices with different strength (ii) Streamwise alignment: 30°–67° (iii) Spanwise spacing: $35\delta_v$–$50\delta_v$ (iv) $\tau_{xy} = 1.6$–3 (v) $d\tau_{yz}/dz > 0$	$y+ \in (0, 40)$ $\langle y^+ \rangle = 25$	10–20	>900
Multiple vortices (including single)	92 (36 %)	(i) Multiple streamwise vortices (ii) No apparent correlative flow and stress distribution associated (iii) Alignment angle: 10°–30° (iv) $\tau_{xy} = 0.8$–1.9	$y^+ = 5$–12	5–30	300–600
Hairpin-like Vortices	6 (2 %)	(i) Hairpin-like structure in the inner layer (ii) Inclination angle >45° (iii) $\mathrm{Max}(\tau_{xy}) = 1.6$–$1.8$ (iv) $\mathrm{Min}(\tau_{xy}) = 0.6$–$0.8$ (v) Spacing: $\sim 50\delta_v$	$y^+ < 50$	5–10	>900
High lying vortices	85 (34 %)	(i) Large-scale structure lies in upper part of buffer layer (ii) No clear correlation with flow and wall stress distribution (iii) $\tau_{xy} = 0.8$–1.2 (iv) Alignment angle: <12°	$y^+ > 45$	>40	200–400

TABLE 2. Rudimentary characterization of near-wall flow structures.

3.2.1. *Counter-rotating pair of streamwise vortices*

Structures similar to those shown in figure 4(*a*) appear in 69 of the 250 realizations (27.6 %). In this sample, all the displayed vortex lines (cylindrical tubes) are initiated at $y^+ = 5$ and $z^+ = 75$, with x^+ varying from 0 to 85 at a spacing of 2.5. Also shown are an isosurface of $\lambda_2 = -480$ and a distribution of the streamwise wall shear stress. These pairs of vortices often seem to originate from the wall and then quickly lift off while being inclined at various angles. Near the wall, the angle with

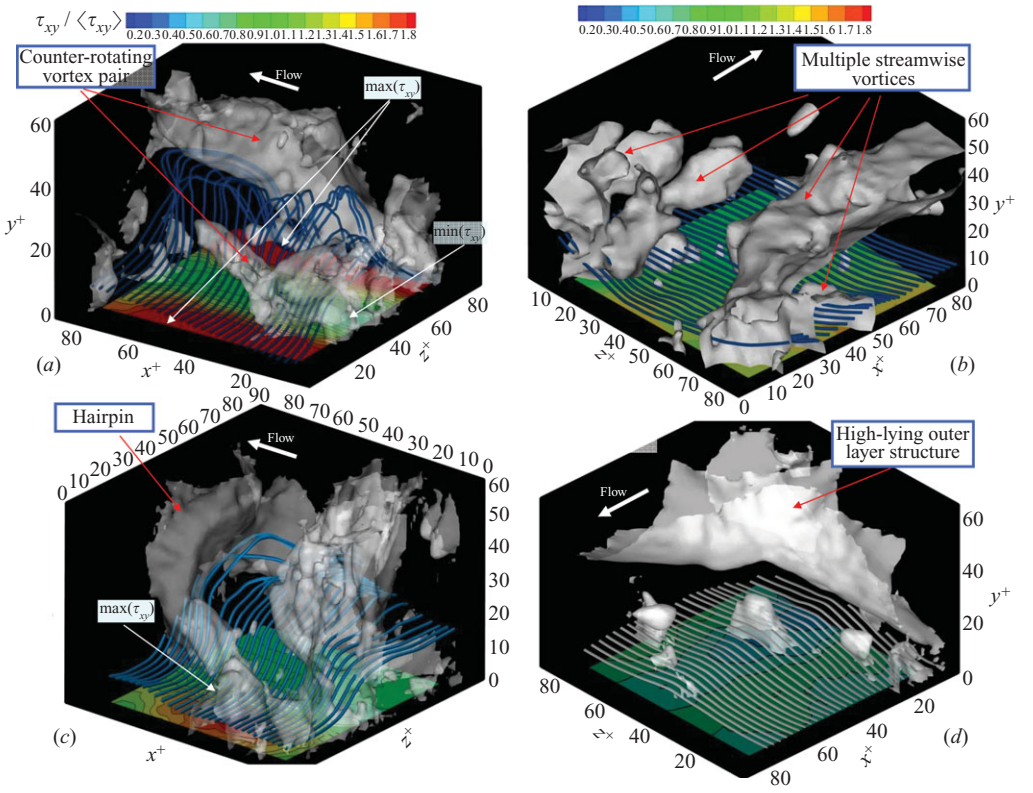

FIGURE 4. Sample instantaneous distributions of λ_2 isosurfaces, wall shear stress and vortex lines, as defined in the text: (*a*) for a counter-rotating vortex pair, $\lambda_2 = -480$; (*b*) for multiple streamwise vortices, $\lambda_2 = -775$; (*c*) for a hairpin, $\lambda_2 = -530$; and (*d*) for high-lying outer layer structure, $\lambda_2 = -665$. Note that the samples are presented at different angles in order to provide the clearest illustration of the flow phenomena involved.

the streamwise axis frequently exceeds 45°. The centres of these pairs are located at $3 < y^+ < 40$ but mostly around $y^+ = 20$, and the spacing between them is $z^+ = 50$–70. Their normalized streamwise vorticity $\omega_x \delta/u_\tau$ often exceeds 1000. In 28 (11 %) of the (total) realizations, the flow induced by a pair is downward; i.e. they generate a stagnation-like 'splatting' flow and a stress maximum on the wall. In 41 (16 %) of the cases, the pairs generate an anti-splatting flow away from the wall, and there is a wall stress minimum between them, as illustrated in figure 4(*a*). Similar to this sample (statistics follows), a local τ_{xy} minimum is typically bounded by maxima on both sides, but they are staggered in the streamwise direction; i.e. the local minimum is located upstream of the local maximum. Near the stress minimum, the structures are still located very close to the wall, and the vortex lines are aligned upward, at an angle of almost 90°. As the structures lift away from the wall, the shear stress between them starts to recover; the vortex lines turn downstream; and the high-shear-stress zones on both sides of the minimum begin to peak. The origin, flow and turbulence associated with these structures are the main foci of this paper, as discussed in § 3 and § 4.

3.2.2. *Multiple quasi-streamwise vortices*

In 92 (36 %) of the cases, multiple quasi-streamwise vortices coexist within the buffer layer and contribute about 35 % of the mean wall shear stress. Figure 4(*b*) provides

a sample three-dimensional depiction of at least four coexisting quasi-streamwise vortices. Flow and vorticity cross-sections for this sample (not shown) reveal that one of the vortices is situated very close to the wall, initially at $y^+ \sim 5$. They also provide evidence for complex vortex–vortex interactions, e.g. vortices interlacing around each other, and vortex–wall interactions, e.g. lateral movement near the wall, even within the viscous and buffer layers. The vortex lines initiated at $y^+ = 5$, $z^+ = 20$ do not show significant deviations away from the wall, and occasional slight depressions and bulging do not involve significant modifications to the wall shear stress.

Examination of all relevant data indicates that structures in this category are primarily aligned in the streamwise direction, with typical tilting angles of less than 20° and a much wider range of spanwise orientations compared to the counter-rotating pairs. They also have a wide variety of spatial arrangements, and the spacing between vortices range from $5\delta_\upsilon$ to $90\delta_\upsilon$. There seems to be no correspondence in magnitude and direction of rotation of neighbouring vortices. Their core sizes, as estimated based on the magnitude of λ_2, vary from $5\delta_\upsilon$ to $30\delta_\upsilon$ in the $y^+ = 5$–12 range but extend to 20–$40\delta_\upsilon$ in the upper parts of the buffer layer. The values of $\omega_x \delta / u_\tau$ within these structures range from –600 to 600, i.e. lower than the counter-rotating pairs. The spatial distributions of wall stresses beneath multiple streamwise vortices do not always display clear causal relationships. However, in cases with vortices located close to the wall, they leave clear 'footprints' on the wall stresses, some of them very large. We examine the structure and impact of these vortices and compare them to previously observed similar phenomena in § 4.3 and § 5.

3.2.3. *Cases with almost no buffer layer structures*

In 85 of the 250 cases (34 %), the sample volume does not have any distinct 'small' buffer layer structures with values of λ_2 exceeding -200. In some of them there is evidence of induced motion by structures that are larger than the sample volume, e.g. a sweeping flow or circular motion caused by vortices located above the sample. The associated wall stress magnitudes vary substantially from instance to instance, but the spatial fluctuations within our measurement domain remain small. Figure 4(*d*) shows a sample containing a large-scale structure with a size of $\sim 40\delta_\upsilon$ passing over the test volume at a distance of $\sim 50\delta_\upsilon$ away from the wall. The near-wall vortex lines remain close to the wall, and the streamwise wall shear stress distribution remains nearly uniform.

3.2.4. *Quasi-spanwise structures*

Spanwise structures residing entirely in the buffer layer are rare, only six (2.4 %), in the present set, but they do exist. Consequently, we cannot attach statistical significance to this phenomenon. A snapshot of a newly generated 'hairpin' is present in figure 4(*c*), and a sample (y, z) cut through this structure, showing velocity vectors and wall stress, is shown in figure 5. This hairpin has a shape of an 'Ω' whose legs are deeply embedded in the buffer layer. The legs are initially aligned with the spanwise direction and then turn upward at an angle of 45° to the streamwise direction. Other sections through this flow (not shown) demonstrate the characteristic roll-up of a hairpin head and a Q2 event with a saddle point below and upstream of the head, consistent with the signature of a hairpin (Adrian *et al.* 2000). While the legs of the hairpin abruptly eject the vortex lines away from the viscous layer to the upper buffer layer, near the head the lines are pushed upstream by the Q2 flow. Upstream of the saddle point, there is another large spanwise structure, which generates a strong Q4

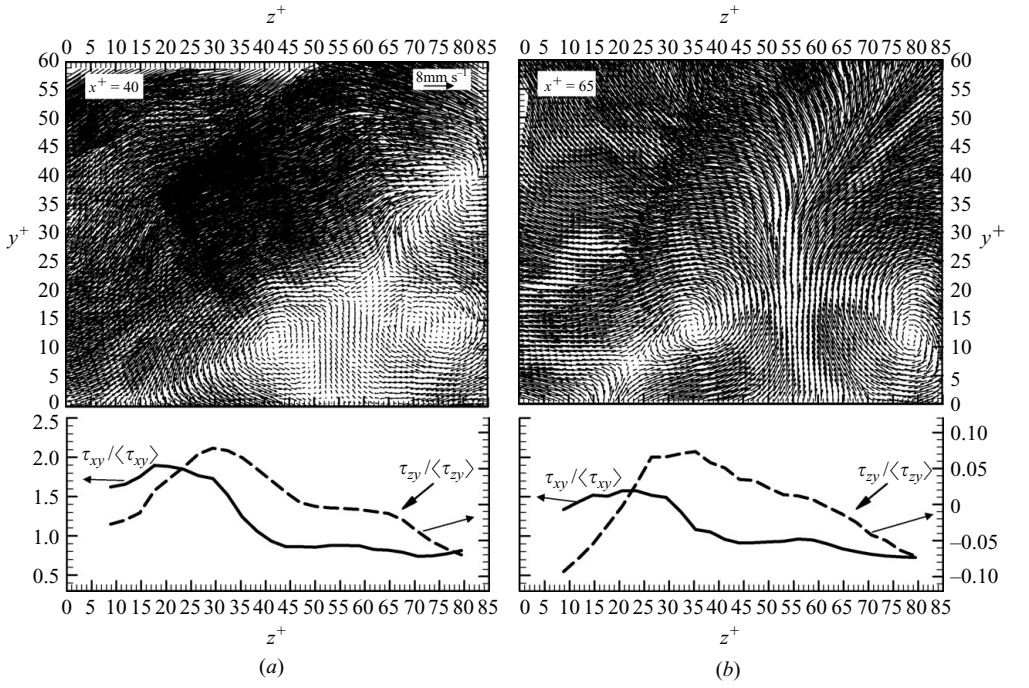

FIGURE 5. Velocity maps in y–z plane and wall stresses under them for the hairpin shown in figure 4(*c*); (*a*) $x^+ = 40$; (*b*) $x^+ = 65$. Dashed line: $\tau_{zy}/\langle\tau_{xy}\rangle$ with the scale on right side; solid line: $\tau_{xy}/\langle\tau_{xy}\rangle$ with the scale on left side.

event above itself. However, due to limitation of our measurement volume, it is not possible to examine it and its relationship with the hairpin (if at all).

4. Flow structures generating extreme stress events revealed by conditional sampling

4.1. *Conditionally averaged wall stress distributions*

To identify and characterize buffer layer structures generating extreme stress events, both maxima and minima, we start by examining the imprint of these structures on the distributions of wall shear stresses. Following procedures introduced in § 2.2, for stress maxima we measure the distributions of

$$\hat{\tau}_{ij}^{max}(\Delta x, 0, \Delta z\ ) = \langle \tau_{ij}(x - x_m, 0, z - z_m) | \tau_{xy}(x_m, 0, z_m) > 1.8\langle\tau_{xy}\rangle \,\&\, \max(\tau_{xy}) = \tau_{xy}(x_m, z_m)\rangle, \quad (4.1)$$

i.e. the distributions of wall stresses for which $\tau_{xy}(x_m, z_m) > 1.8\langle\tau_{xy}\rangle$. For minima, we measure

$$\hat{\tau}_{ij}^{min}(\Delta x, 0, \Delta z\ ) = \langle \tau_{ij}(x - x_m, 0, z - z_m) | \tau_{xy}(x_m, z_m) < 0.6\langle\tau_{xy}\rangle \,\&\, \min(\tau_{xy}) = \tau_{xy}(x_m, z_m)\rangle, \quad (4.2)$$

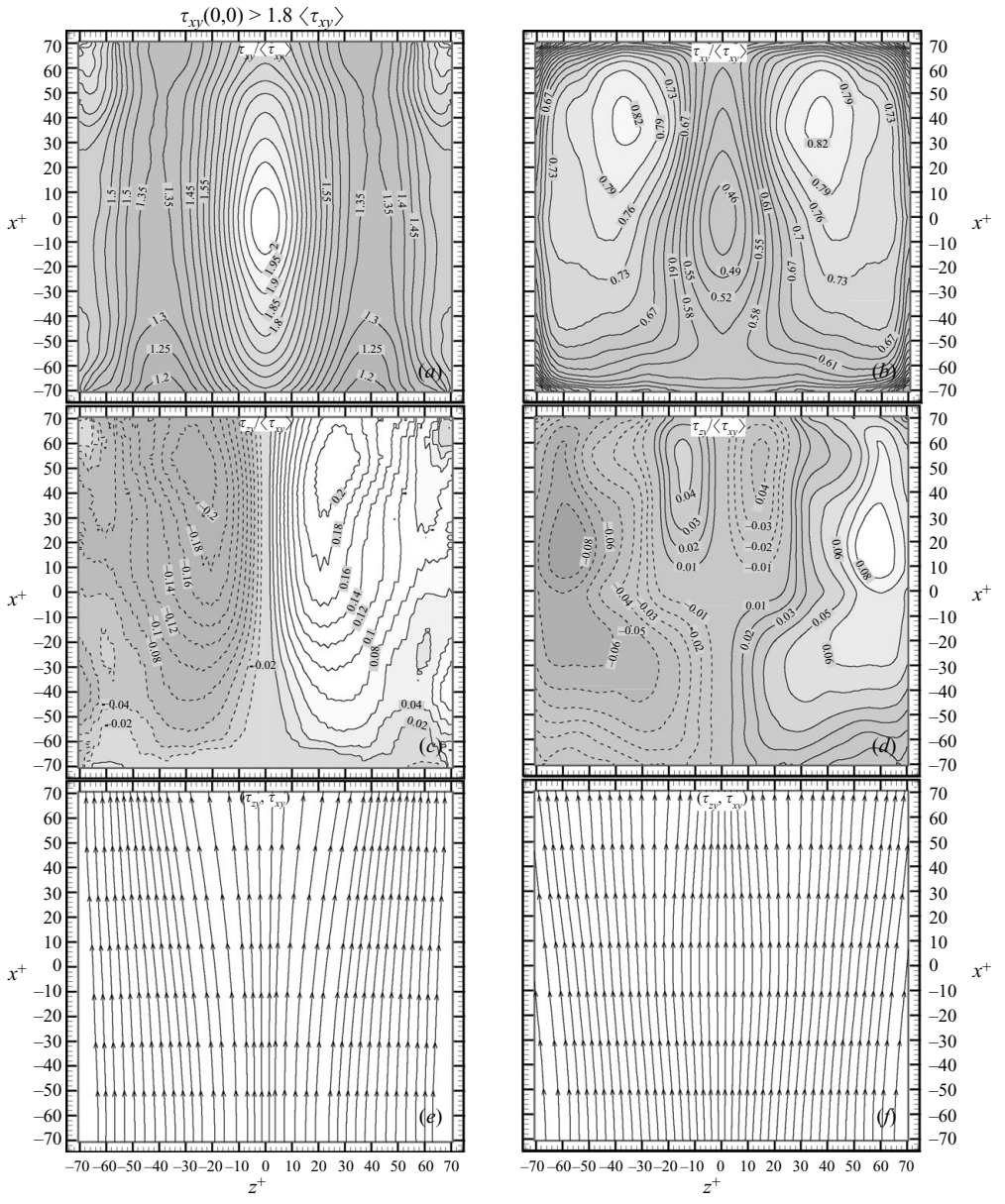

FIGURE 6. Conditionally averaged distributions of wall shear stresses based on high stress, $\tau_{xy} > 1.8\langle\tau_{xy}\rangle$, and low stress, $\tau_{xy} < 0.6\langle\tau_{xy}\rangle$, respectively shown in the left and right panels. In both cases, the conditioned stress extremum is positioned at (0,0). Top row: $\widehat{\tau_{xy}}/\langle\tau_{xy}\rangle$; middle row: $\widehat{\tau_{zy}}/\langle\tau_{xy}\rangle$; bottom row: stress lines of wall shear stress, (τ_{xy}, τ_{zy}). Results are based on analysis of 750 wall stresses and three-dimensional velocity distributions.

i.e. distributions of wall stresses for which $\tau_{xy}(x_m, z_m) < 0.6\langle\tau_{xy}\rangle$. Threshold levels have been selected to maintain sufficient data for averaging while still not smearing features of extreme events. Results are presented in figure 6, the left column for stress maxima, where 297 realizations (39.6 %) of the 750 realizations satisfy our criterion, and the right column for stress minima, where 124 realizations (16.4 %) of

750 satisfy this condition. In both cases, we position the extremum at (0, 0), and for each averaging we use an instantaneous flow field only once. However, as discussed later, significant fraction of the instantaneous data satisfy both criteria but at different locations.

In the vicinity of streamwise stress maximum (figure 6*a*), $\hat{\tau}_{xy}^{max}$ decreases gradually in the streamwise direction and rapidly in the spanwise directions, indicating that spatial coherence is more prominent in the streamwise than the spanwise direction. The elongated low-stress streaks on both sides of the peak, at $z^+ = \pm 35$, contain minima located at least 70 wall units upstream of the maximum, suggesting that the staggered locations of $\hat{\tau}_{xy}^{max}$ extremes, minima and maxima, are related. Shown in figure 6(*c*), $\hat{\tau}_{zy}^{max}$ is 0 at (0, 0) and peaks at $z^+ = \pm 25$ and $x^+ = 45$. A monotonic increase of $\hat{\tau}_{yz}^{max}$ and bell-shaped distribution of $\hat{\tau}_{xy}^{max}$ at a given x^+ indicate divergence of wall stress lines (streamline of wall stress), as figure 6(*e*) confirms. As discussed in § 4.3, this divergence is an imprint of spanwise momentum exchange caused by buffer layer streamwise vortices. We also show that wall stress maxima are generated by two distinctly different types of buffer layer structures.

The elongated minimum in the distribution $\hat{\tau}_{xy}^{min}$ in the vicinity of the stress minimum (figure 6*b*) also indicates larger spatial coherence in the streamwise direction compared to the spanwise direction. However, the minimum is followed by two distinct, staggered stress maxima located near $x^+ = 40$ and $z^+ = \pm 35$. The spanwise stress $\hat{\tau}_{yz}^{min}$, shown in figure 6(*d*), peaks in a region of large streamwise stress gradients, at $z^+ = \pm 15$, $x^+ = 50$, and has two additional peaks with opposite signs at $z^+ = \pm 60$, $x^+ = 20$. As confirmed in figure 6(*f*), these distributions involve convergence of stress lines near and between the inner pair of peaks and divergence in the vicinity of the outer peaks. These patterns indicate that downstream of the streamwise stress minimum, the near-wall flow converges and accelerates in the vicinity of the centreline. We will show in the next section that the staggered, closely located streamwise stress minima and maxima, along with the distributions of spanwise stress, are imprints of the same flow structure that frequently develops in the buffer layer.

Note that the distributions of $\hat{\tau}_{xy}^{max}$ and $\hat{\tau}_{xy}^{min}$ are not symmetric. Although the spanwise spacings between minima and maxima are similar, $z^+ = \pm 35$, the streamwise distance between peaks are clearly different. Furthermore, the maxima in $\hat{\tau}_{xy}^{min}$ downstream of the minimum are distinct, whereas the minima in $\hat{\tau}_{xy}^{max}$ appear only as decreasing trends along a very long streak of low stress. To identify the flow structures involved and explain these differences, we carefully examined 250 of the instantaneous realizations, out of which 91 satisfy the stress maximum condition, and 41 have the required stress minimum.

4.2. *Configuration and impact of structures generating wall stress minima*

This conditional averaging is based on 41 out of the 250 samples (16.4 %), which contain regions with $\tau_{xy} < 0.6\langle\tau_{xy}\rangle$. Figure 7(*a*) presents the conditionally averaged three-dimensional isosurface of $\lambda_2 = -355$ along with the corresponding streamwise wall stress, and figure 7(*b*) shows selected vortex lines. There is a clear agreement of trends of this stress distribution with those shown in figure 6(*b*), which is based on a larger dataset (124 versus 41); i.e. the stress minimum at the origin (by construction) precedes two staggered maxima. As is evident, the dominant averaged structure in the immediate vicinity of stress minimum consists of an inclined pair of counter-rotating, quasi-streamwise vortices that have inclination angles exceeding 45° with the wall. This pair has equal circulation but opposite vorticity signs and generates

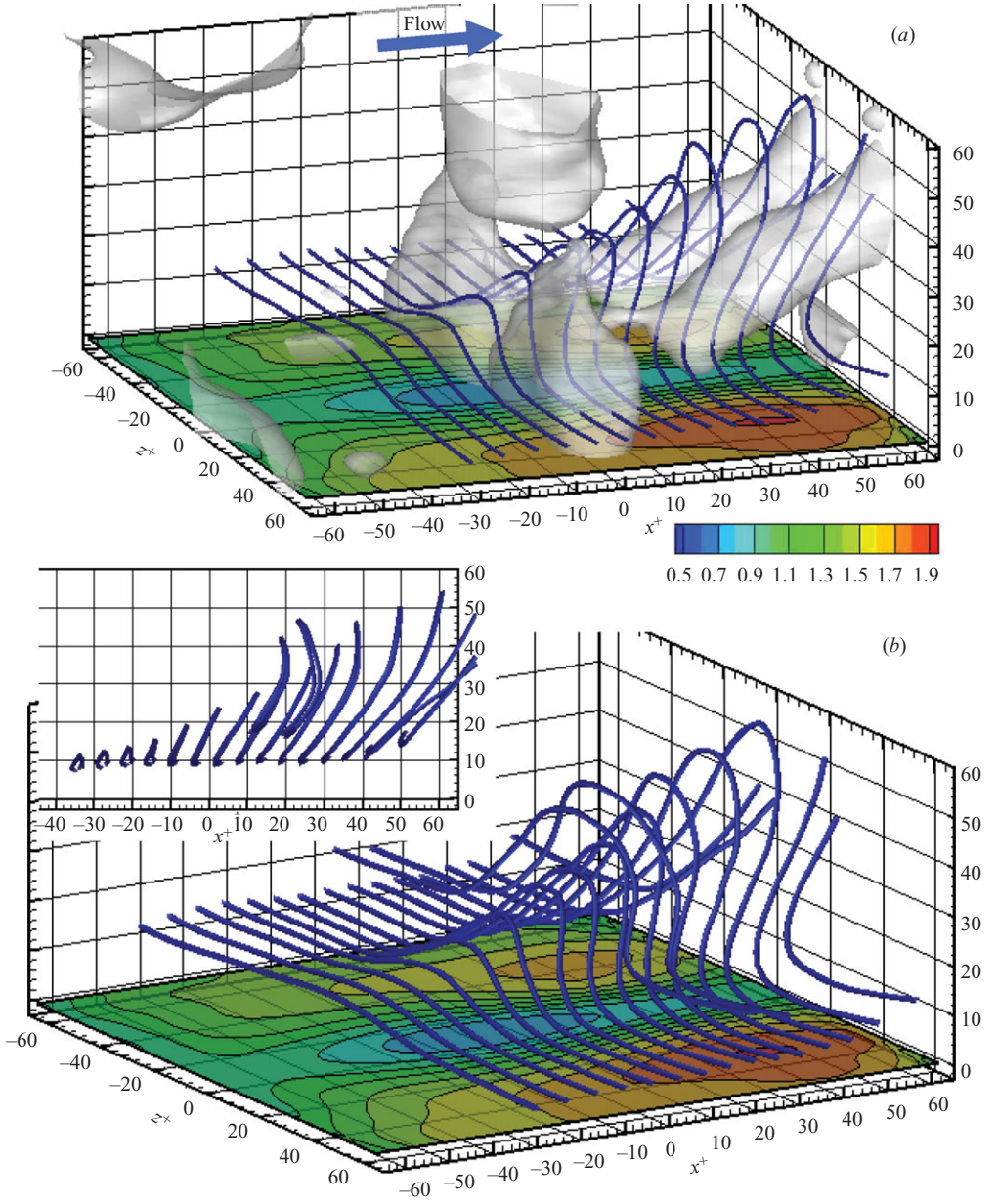

FIGURE 7. Conditionally averaged three-dimensional flow structure and wall stress based on a local stress minimum, $\tau_{xy} < 0.6\langle\tau_{xy}\rangle$, at $x^+ = z^+ = 0$. (*a*) Isosurface of $\lambda_2 = -350$, selected (blue) vortex lines and distribution of $\hat{\tau}_{xy}^{min}(\Delta x, 0, \Delta z)/\langle\tau_{xy}\rangle$. (*b*) Conditionally averaged near-wall vortex lines and distribution of $\hat{\tau}_{xy}^{min}(\Delta x, 0, \Delta z)/\langle\tau_{xy}\rangle$. Insert: x–y projection of the vortex lines.

mostly an 'ejection' ($\widehat{u'^{min}} < 0, \widehat{u'^{min}} > 0$, Q_2 event) between them. For brevity, we will drop the superscript '*min*' in referring to sampling based on stress minimum for the rest of *this* section. The λ_2 plot indicates that two vortices emerge from a region containing spanwise vortices located at $-5 < x^+ < 10$ and are not connected

to any other significant vortical structure located upstream of $x^+ = -10$. These trends persist even when the magnitude of λ_2 is changed (not shown) as long as we maintain high values. The orientation of vortex lines confirm that at $x^+ < -20$ the vorticity near the wall is predominantly aligned in the spanwise direction, with the slight vertical bumps indicating existence of weak vertical vorticity but essentially no streamwise component. Near $x^+ = 0$, the vortex lines lift vertically, consistent with the location of minimum stress point, and subsequently bend slightly in the streamwise directions, as the inclined counter-rotating vortex pair forms. As shown below, the two staggered wall stress maxima appear on the outer side of the vortex pair, in a region influenced by vortex-induced entrainment of fluid with elevated streamwise momentum.

Although individual realizations of the flow and wall shear stress vary significantly, all the features of the conditionally averaged flow appear in 40 of the 41 instantaneous realizations, as illustrated by a sample in figure 8. In addition to the rapidly lifted vortex lines, formation of a vortex pair and its impact are demonstrated by a pair of y–z planes of ω_x, a sample vector map of (w, v) and the corresponding distributions of both wall shear stress components. Lifting of spanwise vorticity to form a counter-rotating vortex pair as well as the resulting formation of stress minimum and staggered maxima are real, frequently occurring buffer layer phenomena. Spanwise vortices turning into streamwise structures have been observed in qualitative flow visualizations at low Reynolds numbers (e.g. Kline *et al.* 1967) or conjectured based on analysis of velocity measurements at limited points (e.g. Robinson 1991). The present results provide clear evidence that these structures indeed exist in high-Reynolds-number boundary layers and demonstrate their impact on the distributions of wall shear stresses.

To elucidate the origin, shape and impact of the structure depicted in figure 7, we examine the flow in several planes dissecting it. Figures 9 and 10 show sample y–z planes of conditionally averaged vorticity. Figures 11 and 12 present streamwise velocity distributions in y–z and x–y planes, respectively, and figures 13 and 14 contain velocity fluctuations and associated Reynolds stresses, also in y–z and x–y planes, respectively. At $x^+ = 0$, the y–z plane of minimum stress, the peaks of $\widehat{\omega_x}$ (figure 9) are less than 15 wall units wide, and their magnitudes are significantly lower than those in the broad region of elevated $\widehat{\omega_y}$. These trends are consistent with the almost vertically lifted sample vortex lines near $x^+ = 0$, as shown in figure 7(b). Even in the area in which vortex lines begin to bend forward, in the vicinity of the $\widehat{\omega_x}$ peak, their angle with the streamwise direction is at least 67°. The peak vorticity magnitude of lifted vortex elements, i.e. $(\widehat{\omega_x}^2 + \widehat{\omega_y}^2)^{0.5}$, is a substantial fraction (70 %) of the local deficit in $\widehat{\omega_z}$ near $z^+ = 0(\widehat{\omega_z}(0, 0, 0) \approx 0.6\langle\omega_z\rangle|_{y=0})$. Ignoring effect of stretching, this agreement supports the argument of lifting and re-orientation of vortex lines, projections of some of which are shown in figure 9(b). At $y^+ > 30$, in the region in which the 'heads' of the lifted vortex lines are aligned horizontally ($-20 < z^+ < 20$), $\widehat{\omega_z}$ is higher than its mean value for that elevation.

Examination of planes located upstream of the abrupt spanwise vorticity lifting, in an attempt to identify precursors to this phenomenon, provides very few clues for what is about to happen. Lack of peaks and very low values of $\widehat{\omega_x}$ in planes located at $x^+ = -30$ and -35 (not shown) indicates that the abrupt lifting is neither preceded nor triggered by a buffer layer streamwise vortex. Consistent with the slight vortex line bumps (figure 7b), $\widehat{\omega_y}\delta/u_\tau$ at $x^+ = -30$ and -35 (also not shown) has broad, low-magnitude peaks in the 50–100 range, i.e. significantly lower than those in the region of vortex lifting (figure 9). Furthermore, as the distributions of $\hat{u}^+$ (figures 11

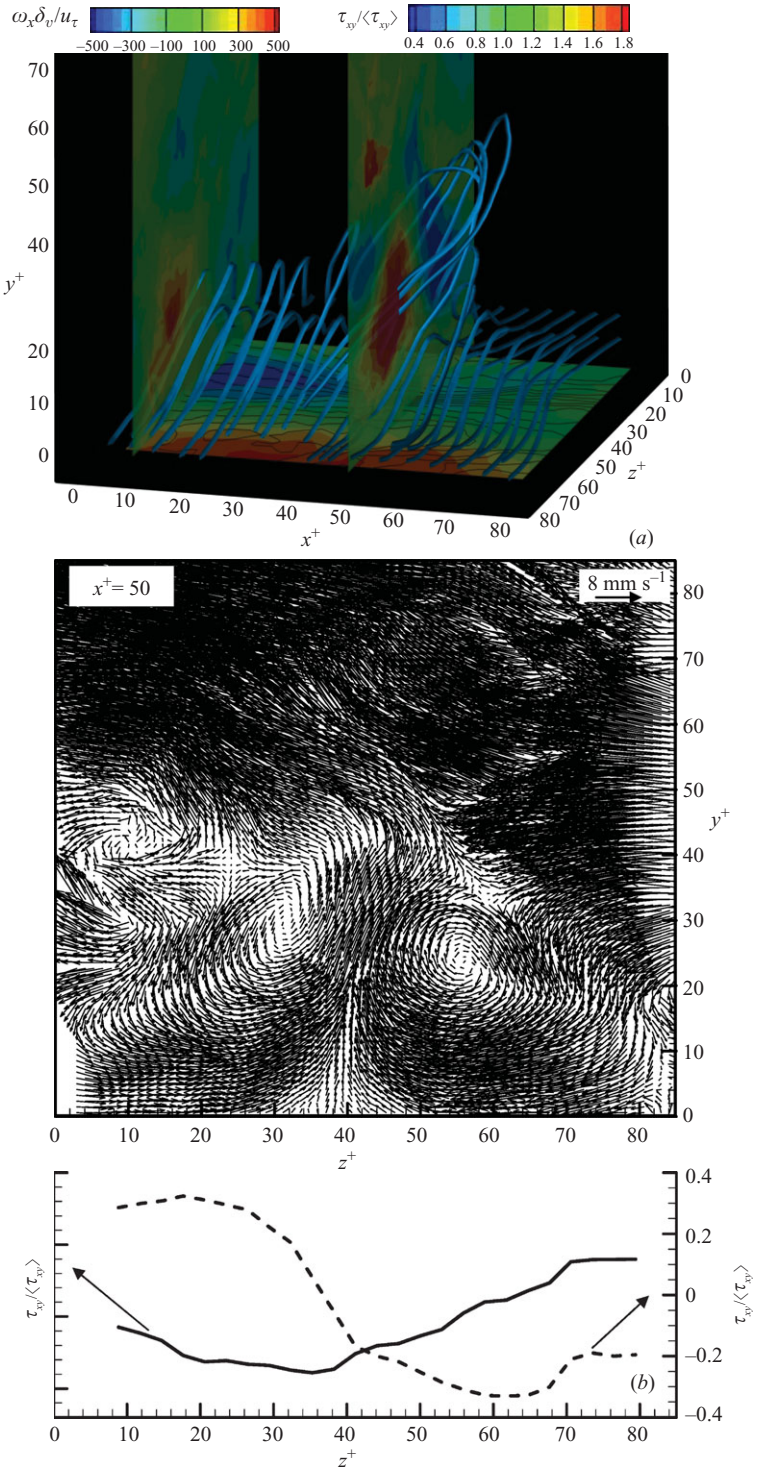

FIGURE 8. A sample instantaneous flow realization satisfying $\tau_{xy} < 0.6\langle\tau_{xy}\rangle$ at some points on the wall. (*a*) Selected vortex lines superimposed with streamwise wall stress and distributions of $\omega_x\delta/u_\tau$ in two planes, $x^+ = 11$ and 50. (*b*) Velocity map in a sample y–z plane, $x^+ = 50$, and the wall stress under it. Dashed line: $\tau_{zy}/\langle\tau_{xy}\rangle$ with the scale on right side; solid line: $\tau_{xy}/\langle\tau_{xy}\rangle$ with the scale on left side.

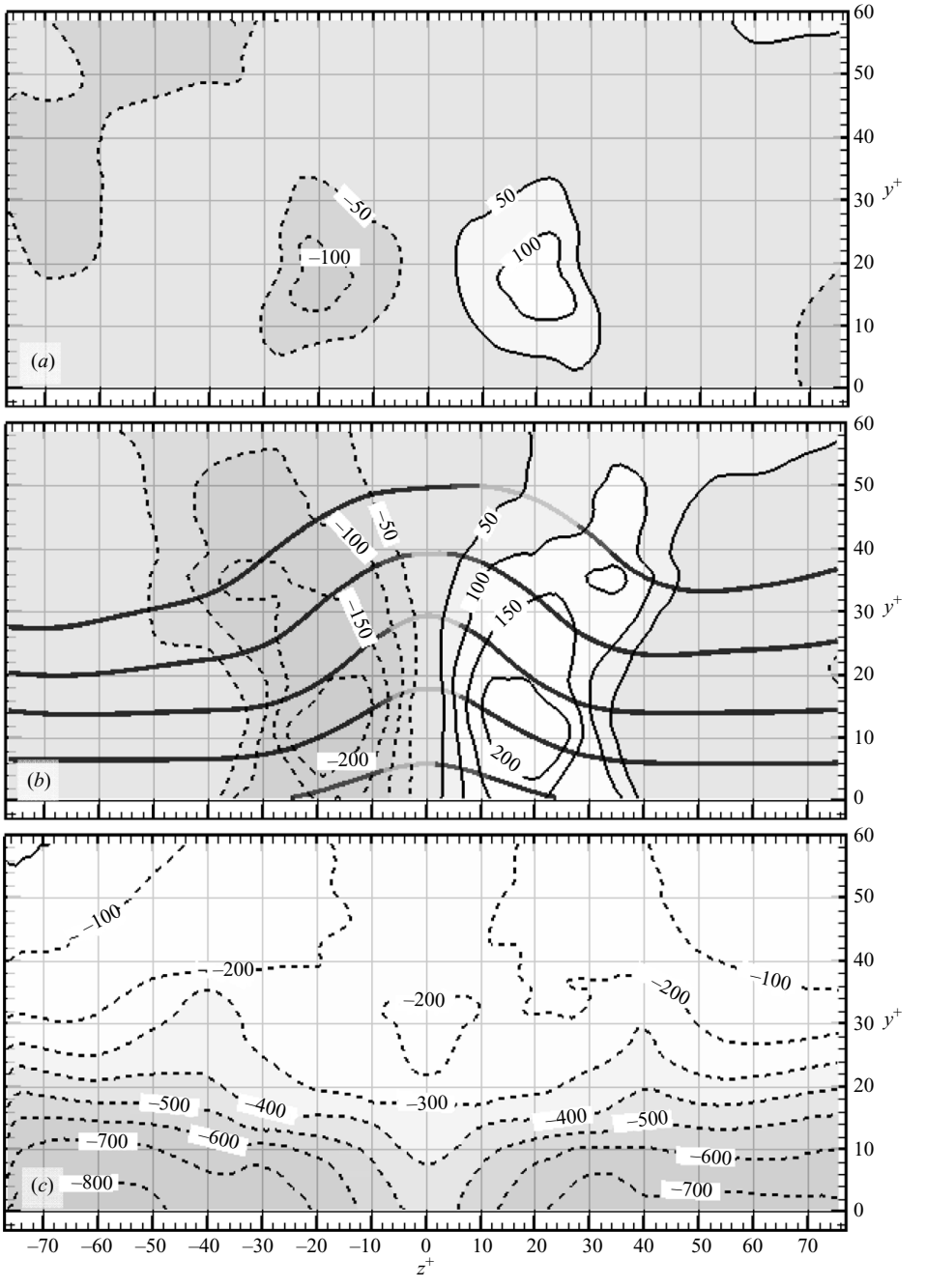

FIGURE 9. Conditionally averaged vorticity components based on a local stress minimum in a y–z plane located at $x^+ = 0$: (*a*) $\widehat{\omega_x^{min}}\delta/u_\tau$, (*b*) $\widehat{\omega_y^{min}}\delta/u_\tau$, (*c*) $\widehat{\omega_z^{min}}\delta/u_\tau$. Contour intervals are 50, 50 and 100, respectively. Also shown are projection of selected vortex lines originating in the $x^+ = -2$ plane. Vortex lines are dark when they are located behind the $x^+ = -0$ plane and light when they are ahead of it.

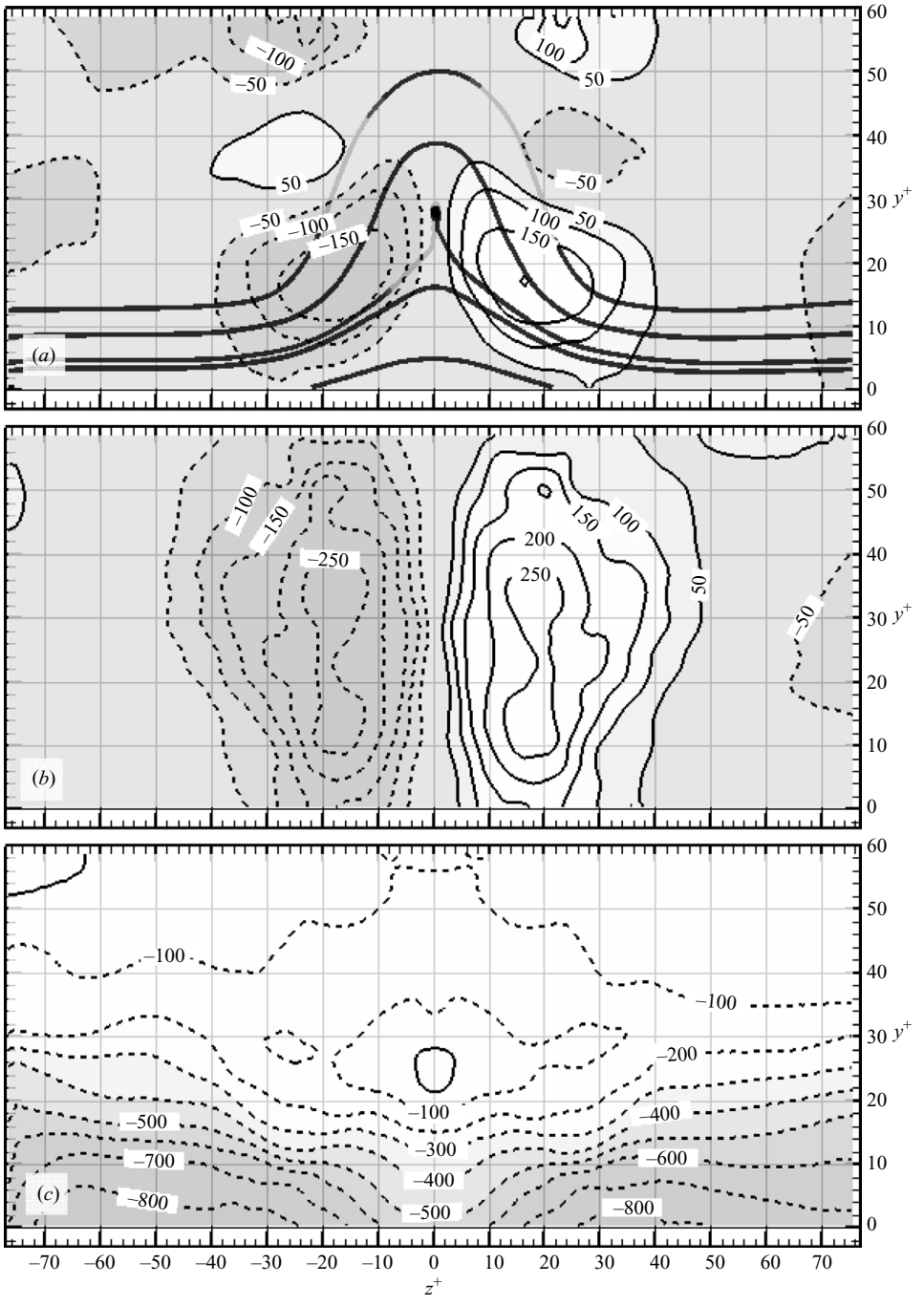

FIGURE 10. Conditionally averaged vorticity components and projection of vortex lines based on a local stress minimum in a y–z plane located at $x^+ = 35$: (*a*) $\widehat{\omega_x^{min}}\delta/u_\tau$, (*b*) $\widehat{\omega_y^{min}}\delta/u_\tau$, (*c*) $\widehat{\omega_z^{min}}\delta/u_\tau$. Contour intervals and vortex line locations are the same as in figure 9

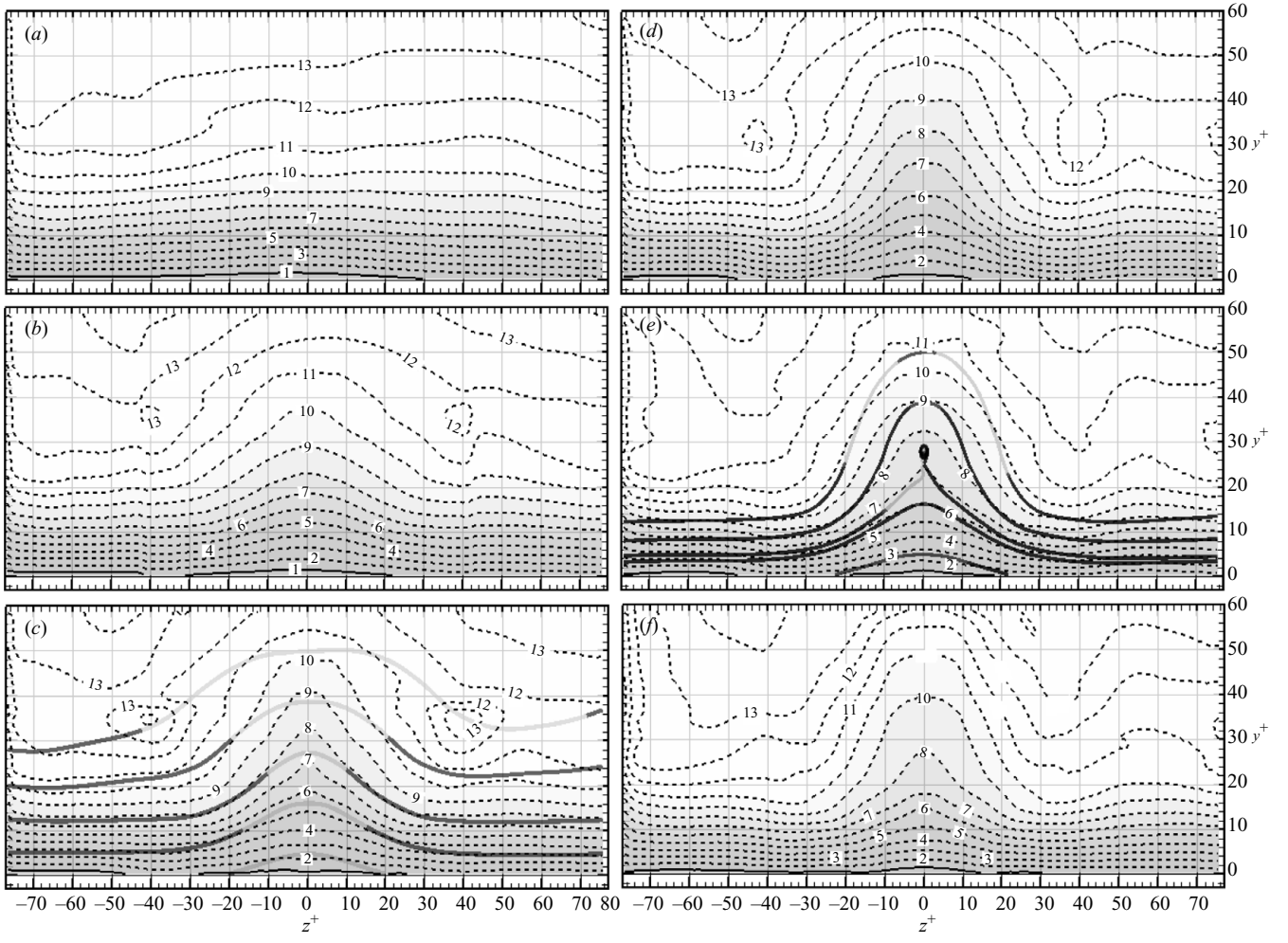

FIGURE 11. Conditionally averaged mean streamwise velocity component $(\widehat{u^{min}}/u_\tau)$ based on local stress minimum in y–z planes located at (*a*) $x^+ = -45$, (*b*) $x^+ = -10$, (*c*) $x^+ = 0$, (*d*) $x^+ = 15$, (*e*) $x^+ = 35$, (*f*) $x^+ = 55$. Contour interval is 1. Also shown are selected vortex lines at $x^+ = 0$ and 35.

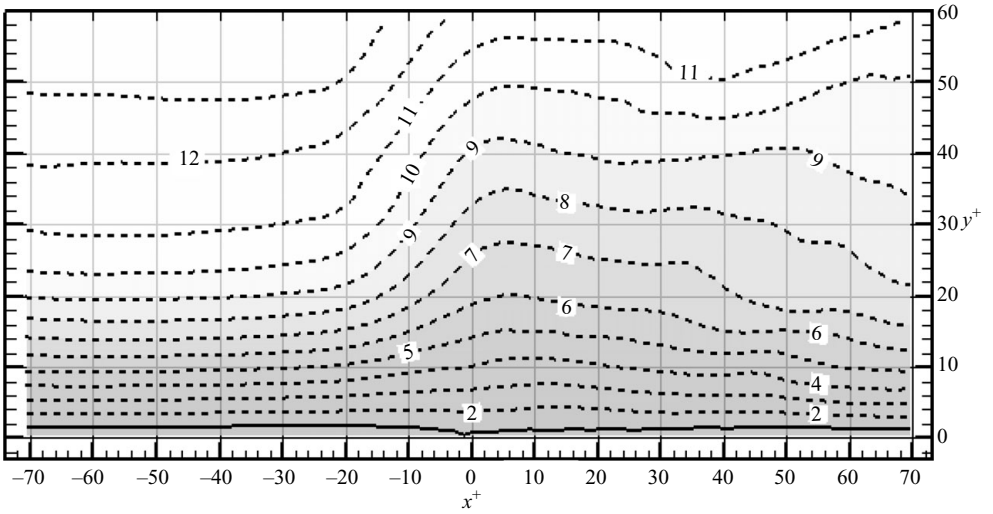

FIGURE 12. Distribution of $\widehat{u^{min}}/u_\tau$ in an x–y plane located at $z^+ = 0$. Contour interval is 1.

and 12) demonstrate, most of the streamwise momentum deficit associated with vortex lifting develops in the $-20 < x^+ < 0$ range. However, $\hat{u}^+$ is lower than its mean values over the entire $x^+ < -10$ space, as is evident from the negative values of $\widehat{u'}$, the conditionally averaged streamwise velocity fluctuation (figures 13 and 14). Thus, the abrupt vortex lifting seems to start in a region of mildly reduced streamwise velocity. This mild deficit is not sufficient for creating an inflection point in the streamwise velocity profiles (not shown), suggesting that the rapid lifting of the vortices is not caused by the instability mechanism described by Acarlar & Smith (1987). We cannot determine the streamwise extent of this reduced velocity region and whether it is part of a low-speed streak, which according to Jimenez & Pinelli (1999) involves periodic abrupt breakup.

The substantial streamwise velocity deficit associated with rapid vortex lifting is evident at $x^+ = -10$ (figures 11*b* and 12) but becomes severe at $x^+ \sim 0$ (figures 11*c* and 12). Here, the low-momentum region has a spanwise extent of $70\delta_v$ and height that exceeds our sample area. This deficit seems to be associated predominantly with reverse flow induced by the vertically lifted vortex elements in the interior parts of vortex arch, although the slight forward tilting induces also vertical transport of low-momentum fluid. Figure 11(*c*) also contains a pair of clear 'islands' of elevated $\hat{u}^+$ in the region in which the vertical vortex elements induce forward flow (at $y^+ = 34$, $z^+ = \pm 40$). These islands are also noticeable at $x^+ = -10$ and 15 (figures 11*b* and 11*d*, respectively). Plausible relationship of the presently observed rapid ejection process to the extensively studied bursting phenomenon (e.g. Willmarth & Tu 1967) is discussed in § 5.

Moving to $x^+ = 35$, the plane containing the staggered streamwise wall stress maxima, the vortex lines bend forward and start forming a distinct counter-rotating vortex pair. The streamwise vorticity increases substantially (figure 10), and the vertical component also increases but not to the same extent. The locations of peak $\widehat{\omega_y}$ and $\widehat{\omega_x}$ now coincide, defining a vortex centre at $z^+ \approx \pm 17$ and $y^+ \approx 17$. The orientation of the vortices remains well above 45°, as defined by the core of λ_2 isosurfaces, but the vortex lines (figure 7*b*) and peak values of $\widehat{\omega_y}/\widehat{\omega_x}(\sim 1.67)$ indicate that the

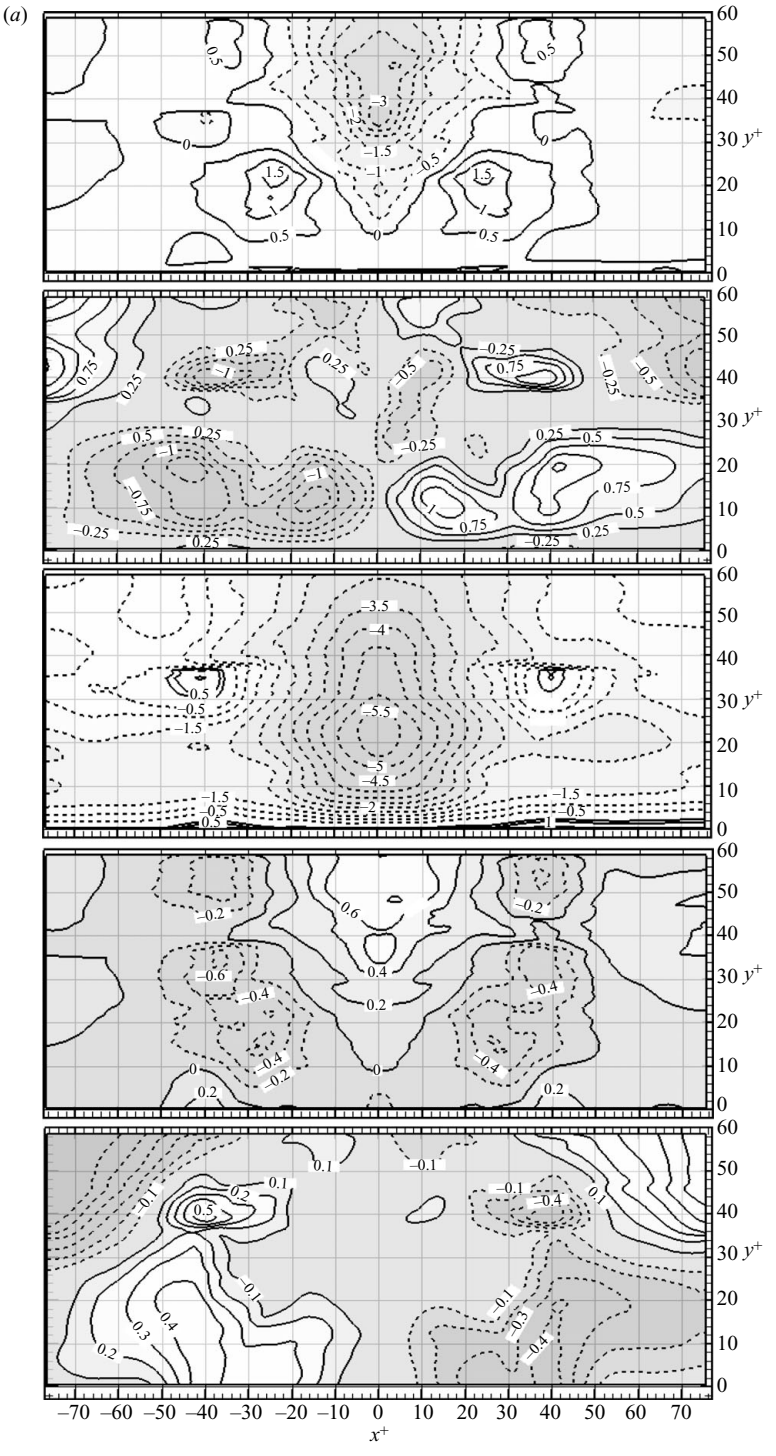

FIGURE 13. For legend see next page.

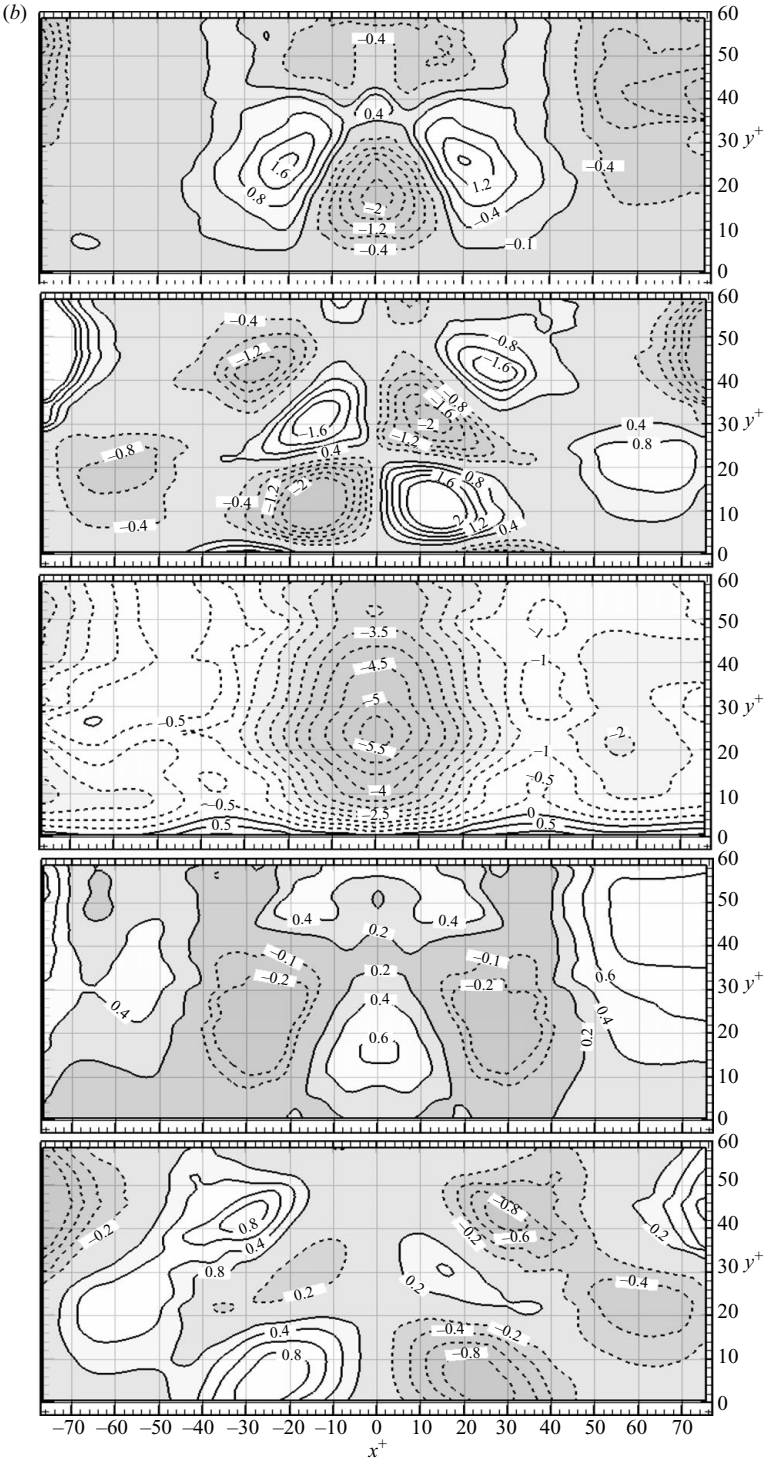

FIGURE 13. Distributions of conditionally averaged velocity fluctuations ($\widehat{u_i'^{min}}$) and Reynolds shear stresses ($u_i'\widehat{u_j'^{min}}$) in y–z planes located at (*a*) $x^+ = 0$ and (*b*) $x^+ = 35$. First row: $\widehat{u'v'^{min}}/u_\tau^2$; second row: $\widehat{u'w'^{min}}/u_\tau^2$; third row: $\widehat{u'^{min}}/u_\tau$; fourth row: $\widehat{v'^{min}}/u_\tau$; fifth row: $\widehat{w'^{min}}/u_\tau$. Corresponding contour intervals are 0.4, 0.4, 0.5, 0.2 and 0.2, respectively.

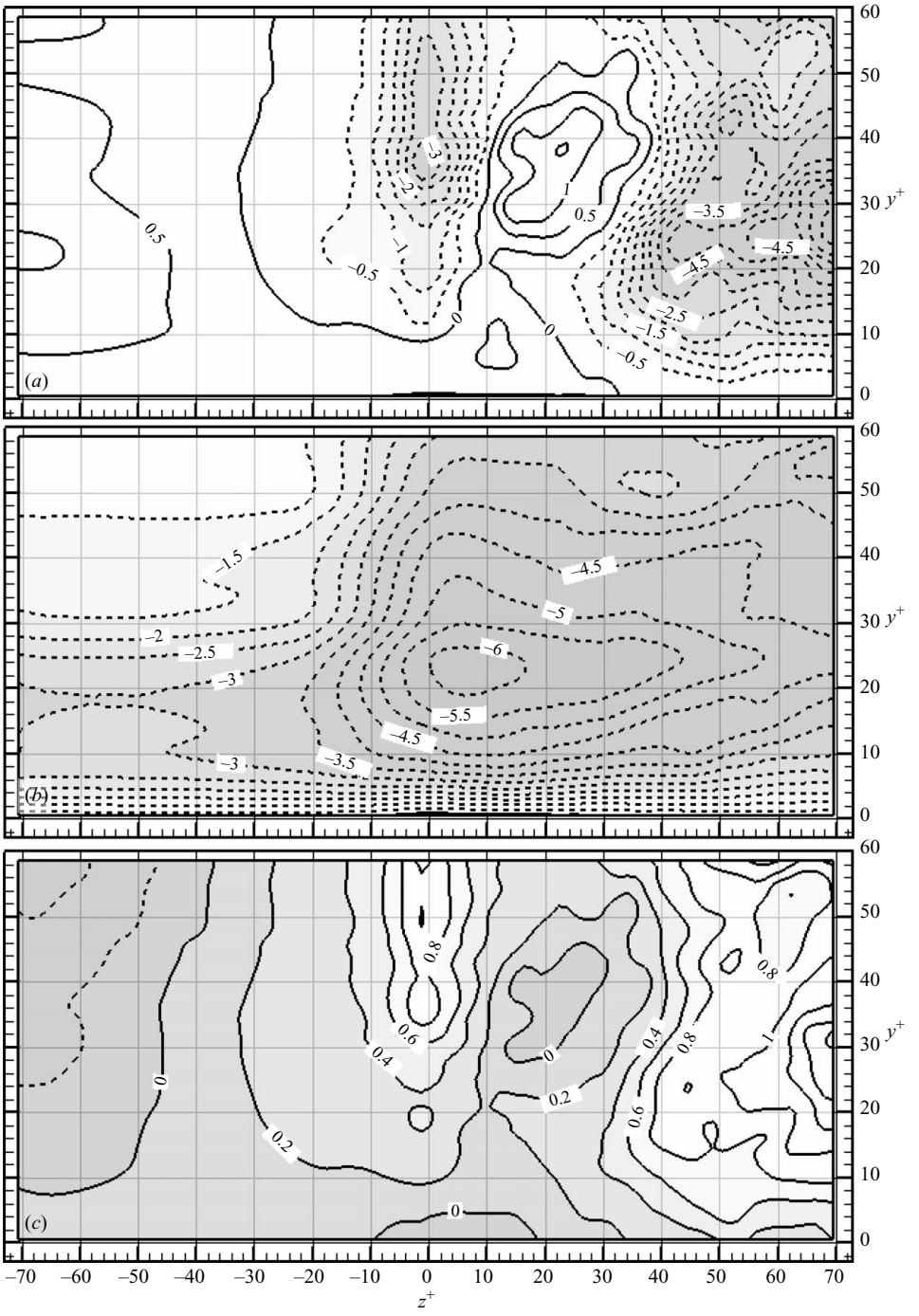

FIGURE 14. Distributions of (*a*) $\widehat{u'v'^{min}}/u_\tau^2$, (*b*) $\widehat{u'^{min}}/u_\tau$ and (*c*) $\widehat{v'^{min}}/u_\tau$, in an x–y plane located at $z^+ = 0$. Contour intervals are 0.5, 0.5 and 0.2, respectively.

vorticity is aligned at angles exceeding 60°. Above its main maxima, at $y^+ = 35$–44 and $z^+ = \pm 25$, $\widehat{\omega_x}$ reverses its sign for reasons that become obvious by examining the vortex lines (figure 7*b*) and distribution of $\hat{u}^+$ (figure 11). During early stages of development, e.g. at $x^+ = 0$ (figure 11*c*), the heads of the vortex line arches are advected at a velocity that is lower than that of their outer parts or 'legs' (figure 11*c*). Consequently, the arch heads bend backward (see x–y projections in figure 7*b*), causing a reversal in the sign of $\widehat{\omega_x}$. This spatially localized trend may be explained by the entrainment pattern resulting from the turning and lifting of the inclined counter-rotating vortex pair, but we opt to avoid this lengthy discussion. At higher elevation, the magnitude of $\hat{u}^+$ in the vicinity of the head gradually exceeds that in the legs (e.g. figure 11*e*), and the arch heads start bending forward again, reversing the sign of $\widehat{\omega_x}$ again. These sign reversals diminish further downstream, when the arch heads are ejected into a higher-velocity region in the lower parts of the log layer.

Consistent with trends of $\hat{\tau}_{xy}^{min}$ (figures 6 and 7), the plot of $\widehat{\omega_z}$ at $x^+ = 35$ (figure 10) displays near-wall peaks at $|z^+| > 25$. Accordingly, corresponding values of $\widehat{u'}/u_\tau$ (figure 13*b*) become positive in the viscous sublayer, peaking at $z^+ = \pm 35$. To determine the mechanism contributing to this increased near-wall momentum, one can examine the local Reynolds stresses (figures 13*b* and 14*a*). The local values of $\widehat{u'v'}$ are very small, consistent with the proximity to the wall, indicating weak vertical transport. Conversely, the high magnitudes of $\widehat{u'w'}$ indicate that spanwise transport of streamwise momentum plays a significant role in the local dynamics. As the corresponding plot of $\widehat{w'}$ shows, once the quasi-streamwise vortex pair forms and detaches slightly from the surface, it generates inward spanwise flow (towards the centre) below the vortices. This flow brings fluid with higher streamwise momentum from outer areas and shrinks the region with lower $\hat{u}$ (figure 11). Formation of a spanwise shear layer beneath the vortices is consistent with signatures of a quasi-streamwise vortex observed in DNS simulation (Kim *et al.* 1987; Adrian & Moin 1988) and with the present shape of stress lines and distributions of $\hat{\tau}_{yz}^{min}$ (figure 6). Vortex-induced motion is also responsible for the outward $\widehat{w'}$ and reversal in the sign of $\widehat{u'w'}$ above the vortex centres (figure 13*b*), at $20 < y^+ < 40$ and $5 < |z^+| < 25$. At higher elevations, in and above the region in which the heads of the vortex lines are bent backward, the signs of both $\widehat{w'}$ and $\widehat{u'w'}$ change again.

At $x^+ > 35$, spanwise transport of high-momentum fluid under the vortices increases $\hat{u}$ in the viscous sublayer and lower buffer layer ($y^+ < 25$) and shrinks the width of the low-momentum zone (figure 11*f*). Conversely, near $z^+ = 0$, low-momentum fluid from the upper buffer layer ($25 < y^+ < 50$) continues to be ejected further up into the lower portion of logarithmic layer, extending the height of the low-momentum region (figures 11*f* and 12). Associated self-induced upward migration of the vortices or head of vortex lines exposes them to ever-increasing streamwise velocity, which keeps on stretching and bending them forward (figure 7*b*). With the limited spatial extent of our present data, we cannot determine the total height (or length) of the zone with low streamwise momentum, which we expect to continue shrinking in width and whether it is related to low-speed streaks whose spatial and temporal characteristics have been studied extensively (e.g. Kline *et al.* 1967; see discussion in § 5).

Before concluding this section, we briefly discuss the impact of the observed structures on vertical velocity fluctuations and momentum transport. In the central x–y plane (figure 14), there is a region with $\widehat{v'} > 0$ and quite high $-\widehat{u'v'}(-\widehat{u'v'}/u_\tau^2 > 3)$ near $x^+ = 0$, followed by an area with low v' at $5 < x^+ < 30$ and then by a domain with high v' and very high $-\widehat{u'v'}$ further downstream. Ejection near $x^+ = 0$ is associated

with the initial abrupt lifting of vortex lines and resulting formation of streamwise momentum deficit. In this area $\widehat{w'}$ is very small (figure 13*a*); hence an abrupt decrease in $\widehat{u'}$ must involve an increase in $\widehat{v'}$, which is induced and consequently peaks behind the heads of the slightly inclined vortical arches. In a consistent manner, $\widehat{v'}$ becomes negative in areas located outward (to the sides) of the inclined vortical arch legs. Slightly above and outside of the $\widehat{\omega_x}$ peaks in this plane, where the vortex lines have the highest forward inclination, the vortex-induced downward flow generates $\widehat{u'v'} > 0$ peaks, which are centred around $z^+ = \pm 24$ and $y^+ = 22$. Being still located in a region with $\widehat{u'} < 0$, at the periphery of momentum deficit area, the vortex-induced downward flow creates a significant Q3 event ($\widehat{u'} < 0,\ \widehat{v'} < 0$).

In the $5 < x^+ < 35$ and $20 < y^+ < 50$ range, $\widehat{v'}$ is small and $\widehat{u'v'} > 0$, even in the $z^+ = 0$ plane (figure 14). As mentioned before, this region contains distorted vortex lines whose legs tilt forward at low elevations, but their upper parts bend backward due to variations in advection speed (figure 7*b*). Consequently, the direction of vortex-induced vertical momentum flux is reversed. Starting near $x^+ = 35$, as the arch heads bend forward again and the vortex pair forms, ejection becomes dominant in the vicinity of the $z^+ = 0$ plane, and its strength increases with streamwise distance, reaching $\widehat{u'v'}/u_\tau^2 > 5$ at $x^+ = 70$. The y–z plane at $x^+ = 35$ (figure 13*b*) shows an early stage of this ejection. Here, the inclined vortex pair induces $\widehat{v'} > 0$ in the middle and $\widehat{v'} < 0$ on outer sides, as expected. In the latter area, $u'v'$ is positive, since $\widehat{u'} < 0$ almost everywhere (Q3 events), and peaks just outward and above the peaks in $\widehat{\omega_x}$, at the periphery of momentum deficit area. Owing to the orientation of the vortex pair, the peak magnitudes of vortex-induced $\widehat{w'}$ are significantly larger than those of $\widehat{v'}$. However, the magnitudes of $\widehat{u'w'}$ and $\widehat{u'v'}$ peaks are similar; i.e. both play significant role in streamwise momentum transport but obviously not at the same locations. Further downstream (not shown), the influence of the counter-rotating vortices becomes more prominent, e.g. increasing the ejection between them. Furthermore, the Q3 regions on outer sides are replaced by sweeps (Q4), as $\widehat{u'}$ becomes positive due mostly to spanwise entrainment of higher momentum fluid. The multiple $\widehat{u'w'}$ peaks also disappear (not shown), leaving only the signature of intense inward flux under the rising vortices as they reach the top of the sample area.

4.3. *Configuration and impact of structures generating wall stress maxima*

4.3.1. *Three-dimensional flow structures generating stress maxima*

In this section, we examine the flow structure in 91 realizations out of 250 that contain regions satisfying $\tau_{xy} > 1.8\langle\tau_{xy}\rangle$. Figure 15(*a*) displays the conditionally averaged $\hat{\tau}_{xy}^{max}$ and isosurface of $\lambda_2 = -355$. As before, the point of maximum stress is located at $x^+ = z^+ = 0$. The wall stress distribution is consistent with that presented in figure 7(*a*), which is based on a larger sample pool (295 out of 750), but it is less smooth and less symmetric, as expected. A pair of elongated, counter-rotating, very slightly inclined ($\sim 8^\circ$) vortices that generate a splatting flow (downwash) between them resides on both sides of the stress maximum. The centres of these vortices are located at $z^+ = \pm 20$ and rise from $y^+ = 20$ at $x^+ = 0$ to $y^+ = 25$ at $x^+ = 35$. A second pair of weaker vortices rotating in opposite direction have centres located at $z^+ = \pm 65$ and vary in height from $y^+ = 40$ at $x^+ = 0$ to $y^+ = 55$ at $x^+ = 35$, i.e. an inclination angle of 23°. Corresponding three-dimensional distributions and projections of selected vortex lines (figure 15*b*) show two regions of lifted vortex lines with 'Ω-shaped' heads on both sides of the maximum. They are subsequently stretched and bent forward, each bearing resemblance to the structure discussed in the previous

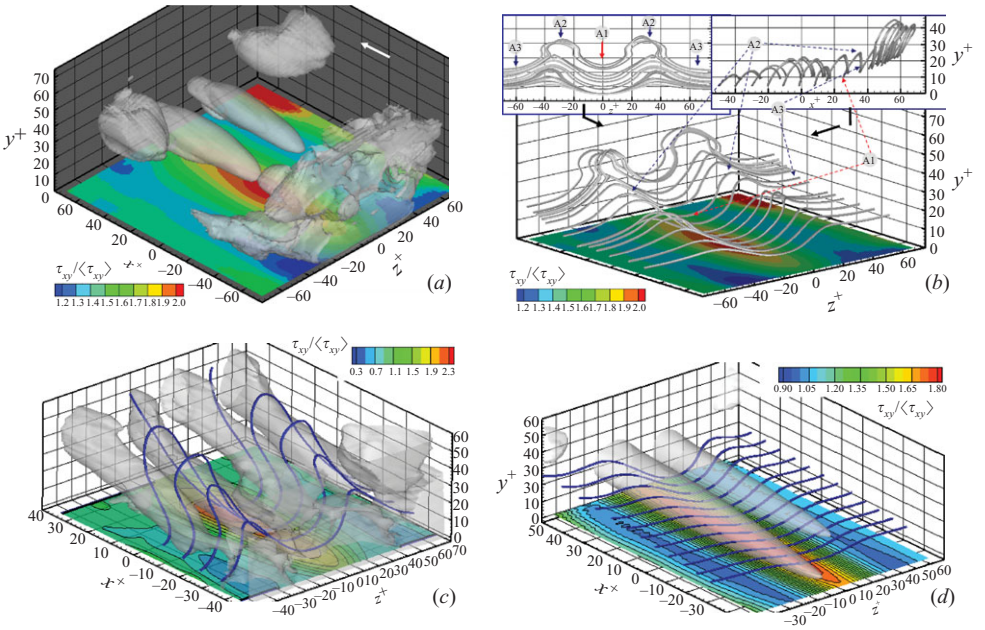

FIGURE 15. Conditionally averaged three-dimensional flow structure and wall stress based on a local stress maximum, $\tau_{xy} > 1.8\langle\tau_{xy}\rangle$, at $x^+ = z^+ = 0$. (*a*) Isosurface of $\lambda_2 = -355$ and distribution of $\hat{\tau}_{xy}^{max}(\Delta x, 0, \Delta z)/\langle\tau_{xy}\rangle$. (*b*) Selected conditionally averaged near-wall vortex lines and distribution of $\hat{\tau}_{xy}^{max}(\Delta x, 0, \Delta z)/\langle\tau_{xy}\rangle$. Left insert: y–z projection; right insert: x–y projection of these vortex lines. Labels show corresponding points in different views. (*c*) Conditionally averaged $\lambda_2 = -355$ isosurface, wall stress and selected vortex lines based on a local stress maximum with a staggered minimum located upstream of it. (*d*) Conditionally averaged $\lambda_2 = -355$ isosurface, wall stress and selected vortex lines when the stress maximum is not preceded by a staggered minimum.

section. The presence of staggered wall stress minima upstream of the maximum also supports this initial impression. However, there are also distinct differences, e.g. the alignment of λ_2 isosurfaces, and the streamwise distance between wall stress maxima and minima (see figure 6). Also, vortex lines are aligned differently. Here, the outer parts of vortex lines in the vicinity of the stress maximum (marked as A3 in figure 15*b*) are located downstream of the arch heads (A2), and in the centre (A1), the vortex lines are pushed towards the wall and lag significantly behind other parts.

In an attempt to explain the similarities and discrepancies between the flows presented in figures 7 and 15(*a*), we have examined each of the 91 realizations and have found that two distinctly different flow structures generate wall shear stress maxima. The first group includes 40 of the 41 realizations discussed in §4.2 and is characterized by a wall stress minimum located upstream of a pair of staggered stress maxima. When we use this set to plot the conditionally averaged three-dimensional flow based on the location of stress maximum, we obtain the structure shown in figure 15(*c*). Since the averaging procedure positions the stronger of the two stress maxima associated with each vortex pair at the origin, the counter-rotating pair may be located to the right or left of the stress maximum, depending on which maximum is stronger. Consequently, figure 15(*c*) contains two laterally shifted duplications of the vortex pair displayed in figure 7. As expected, for this group, the λ_2 isosurfaces have inclination angles exceeding 45°; the vortex lines are inclined at ∼64°; and the

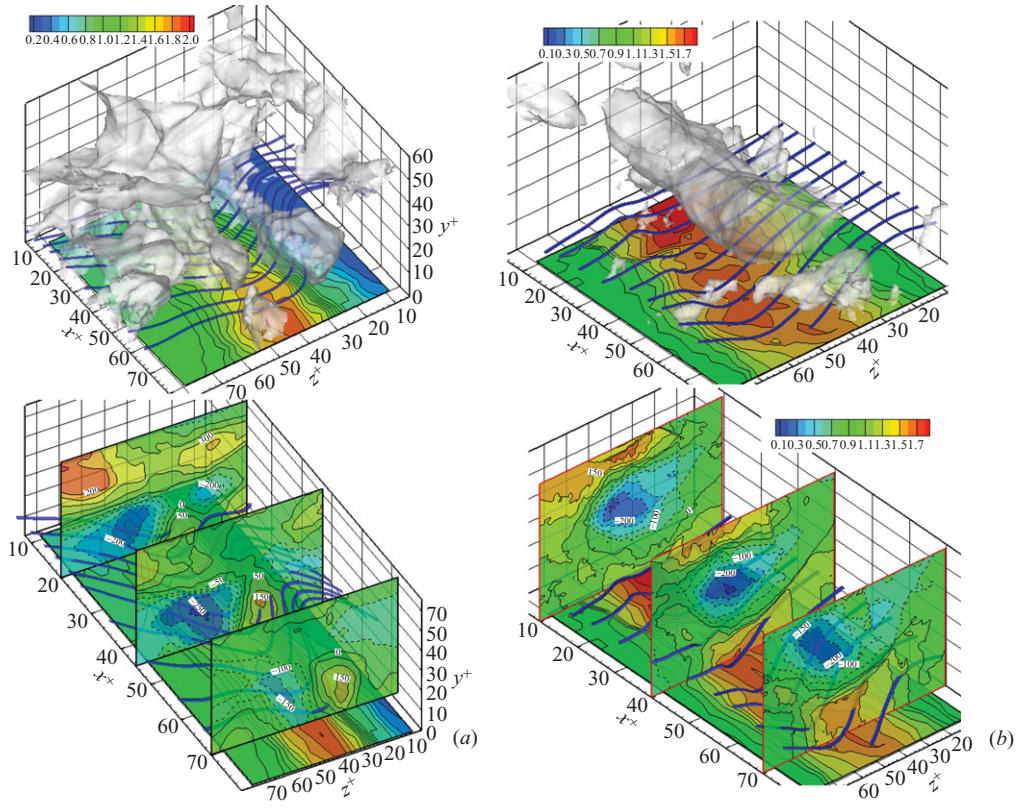

FIGURE 16. Sample instantaneous isosurfaces of λ_2 (top), vortex lines, $\tau_{xy}/\langle\tau_{xy}\rangle$ and $\omega_x\delta/u_\tau$ (bottom) of (*a*) a $\lambda_2 = -440$ isosurface of a pair of streamwise vortices generating a splatting flow between them and (*b*) single buffer layer vortex generating a stress maximum depicted using $\lambda_2 = -510$.

streamwise distance between stress maximum and minima is reduced to about $35\delta_\upsilon$. However, the spanwise distance between stress minima in figure 15(*c*), $\sim 100\delta_\upsilon$, is significantly larger than the distance between maxima, $70\delta_\upsilon$, as shown in figure 7. Considering that both are based on almost the same data (40 of 41 cases), this difference must be associated with the conditional-averaging procedure. Since there are variations in the rise rate and orientation of vortices in an instantaneous pair, on average the vortex that generates a higher wall stress peak must also migrates further in the spanwise direction from the stress minimum. A plausible explanation for this trend is that the vortex that lingers for a longer time near the bottom generates a higher stress and migrates further outward due to stronger interaction with the wall (higher induced flow by its image).

Without the prior knowledge (§ 4.2), the phenomenon depicted in figure 15(*c*) would give an impression that the stress maximum is generated as a sweeping (splatting) flow between the two central pair of inclined structures and injects high-momentum fluid towards the wall. However, although a splatting pair of vortices has been observed in 28 out of 250 instantaneous realizations (table 2), only seven of them satisfy the stress magnitude criterion ($\tau_{xy} > 1.8\langle\tau_{xy}\rangle$). Furthermore, they are never symmetric, and as the sample in figure 16(*a*) shows, lifting of vortex lines and generation of stress maximum and minimum are associated with the structure on the right side,

whereas the presence of the second vortex on the left is coincidental. We have not found even one instantaneous flow field showing a pair of vortices with similar circulation generating a splatting flow between them. However, 5 out of the 91 (stress maximum) realizations contain four vortices, consisting of two dissimilar pairs, with a wall stress peak between the two inner vortices. In this case, we believe that each side contains an independent pair, and they happen to lie near each other. A flow consisting of four very similar vortices, as shown in figure 15(*c*), is an artefact of the conditional-averaging procedures.

The conditionally averaged flow structure of the second group of 51 (out of 250) realizations satisfying the stress maximum condition is depicted in figure 15(*d*). This flow consists of a pair of low-lying streamwise vortices, which are inclined at 12° with the streamwise direction and generate a splatting flow between them. Instantaneous distributions associated with this group, a typical sample of which is presented in figure 16(*b*), show that the stress maximum is generated by a single vortex. Formation of the conditionally averaged splatting pair is an artefact of the sampling procedure, which places the vortices on both sides of the stress maximum. The averaged vortex lines also remain close to the wall, dipping only slightly towards the wall and backward above the high-stress region, indicating, as will be demonstrated shortly, that formation of a wall stress peak does not involve substantial vertical momentum transport. Instead, the increased wall stress is mostly a result of vortex-induced spanwise transport of fluid into the gap between the vortices and the resulting acceleration of the flow there. The elongated high-wall-stress region is bounded on both sides by long streaks of low stress, which are separated by $\sim 84\delta_\upsilon$. These weak-stress regions have characteristic magnitude of $\sim 0.9 < \tau_{xy} >$; i.e. they are not as low by a wide margin as those occurring when spanwise vorticity abruptly lifts away from the wall (figures 7 and 15*c*). Consequently, except for one case, which is included in the analysis discussed in § 4.2, they do not satisfy the stress minimum criterion ($\tau_{xy} < 0.6\langle\tau_{xy}\rangle$). The role of isolated buffer layer vortices in formation of near-wall low-speed streaks is discussed in many papers (e.g. Kravchenko, Choi & Moin 1993; Jimenez & Pinelli 1999; Schoppa & Hussain 2000, 2002) based on DNS data, and it is likely that we are observing the same phenomenon, as discussed in § 5.

When the wall stress distributions in figures 15(*c*) and 15(*d*) are combined into a single conditional average based on a stress maximum, as shown on the left side of figure 6, the low-lying vortices generate the elongated low-stress streaks, and the lifted vortex pairs generate staggered minima upstream of the maxima. Superposition of these two different flow phenomena creates the puzzling three-dimensional λ_2 isosurfaces and vortex lines shown in figures 15(*a*) and 15(*b*). In the following sections, we briefly discuss each flow phenomenon, while paying more attention to the low-lying vortices, since the lifted vortex pair is already described in detail in § 4.2.

4.3.2. *Sections through low-lying vortices generating stress peaks*

Figures 17(*a*) and 17(*b*) show distributions of $\hat{\omega}_x^{max}\delta/u_\tau$ and $\hat{\omega}_y^{max}\delta/u_\tau$, respectively, within the low-lying vortices in three y–z planes located at $x^{+max} = -35$, 0 and 35. Corresponding distributions of streamwise velocity are presented in figure 17(*c*); velocity fluctuations at $x^+ = 0$ are shown in figure 18(*a–c*) (trends in other planes are sufficiently similar, and there is no point to present them); and Reynolds shear stresses are presented in figure 19. We will omit the superscript '*max*' in the rest of this section for brevity. The plots of $\widehat{\omega_x}$ and $\hat{u}$ also contain projections of sample vortex lines. As is evident from figure 17, the low-lying vortices are embedded deeply within the buffer layer with vortex centre height in the $y^+ = 14$–17 range. Both $\widehat{\omega_x}$ and $\widehat{\omega_y}$ peaks increase

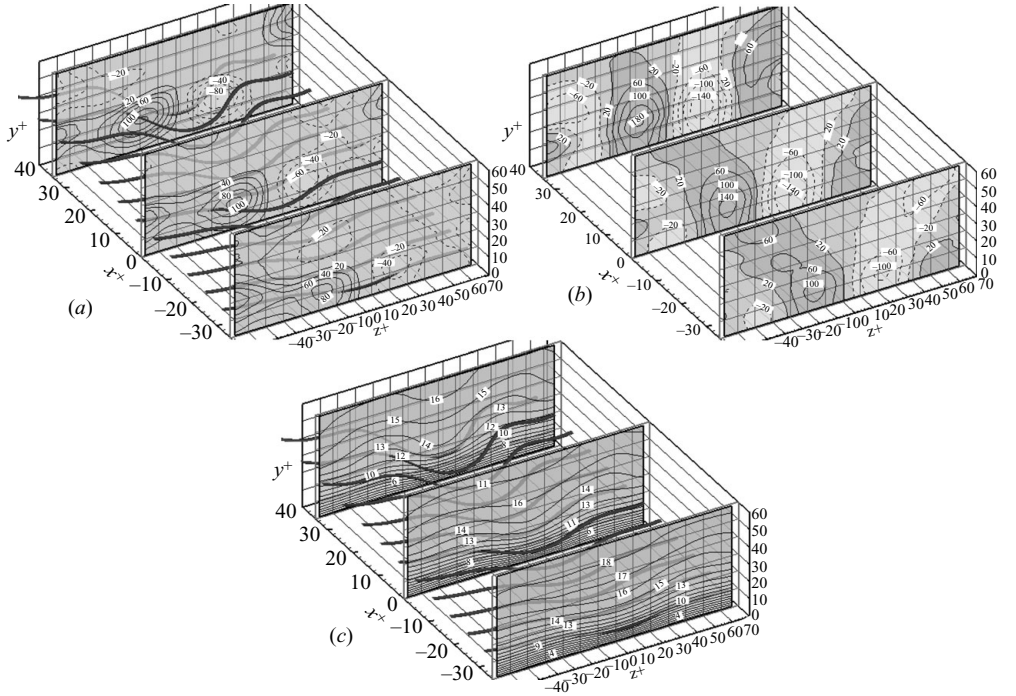

FIGURE 17. Conditionally averaged flow based on local shear stress maximum for realizations containing single, low-lying vortices, without stress minimum upstream (only): (*a*) $\widehat{\omega_x^{max}}\delta/u_\tau$ and (*b*) $\widehat{\omega_y^{max}}\delta/u_\tau$. Contour intervals are 20 and 40, respectively. (*c*) Mean streamwise velocity component, $\widehat{u^{max}}/u_\tau$. Each plot contains three y–z planes located at $x^{+max} = -35$, 0, 35.

with x^+, but $\widehat{\omega_y}/\widehat{\omega_x}$ remains significantly larger than 1, indicating angles exceeding 60° with the streamwise direction. The centre of the vortex is the only region in which vortex lines deviate significantly from the spanwise direction, and even there, they only bend downward and backward (figures 15*d* and 17*a*), consistent with trends of vorticity components. The slight upward bending of vortex lines outward of the main vortices, at $|z^+| > 40$, presumably due to upward flow induced by the vortex, creates regions with elevated $\widehat{\omega_y}$ with opposite signs. Divergence of regions with elevated $\widehat{\omega_y}$ away from the centre at $x^+ = -35$ and 0 (figure 17*b*) show the regions in which vortex lines start bending downward.

As these vortices develop in the streamwise direction, their impact on streamwise momentum extends to higher elevations (figure 17*c*), but most of the changes are still confined to the buffer layer. In fact, vertical momentum flux, as indicated by the values of $\widehat{u'v'}/u_\tau^2$, is weak even within the limited sweep area near the centre (figure 19*a*). Conversely, the spanwise momentum flux $\widehat{u'w'}/u_\tau^2$ is substantial (figure 19*b*), indicating that most of the transport leading to generation of stress maximum is lateral. Below the vortices, at $y^+ < 10$, there is outward flux, as indicated by the sign of $\widehat{w'}$ (figure 18*c*), while above and over a wide area outward of these vortices, they generate inward flux. The substantially higher contributions of $\widehat{u'w'}$ in comparison to $\widehat{u'v'}$ is consistent with the orientation of vortex lines (>60°) near the vortex centres, which inherently induces more horizontal flow than vertical one.

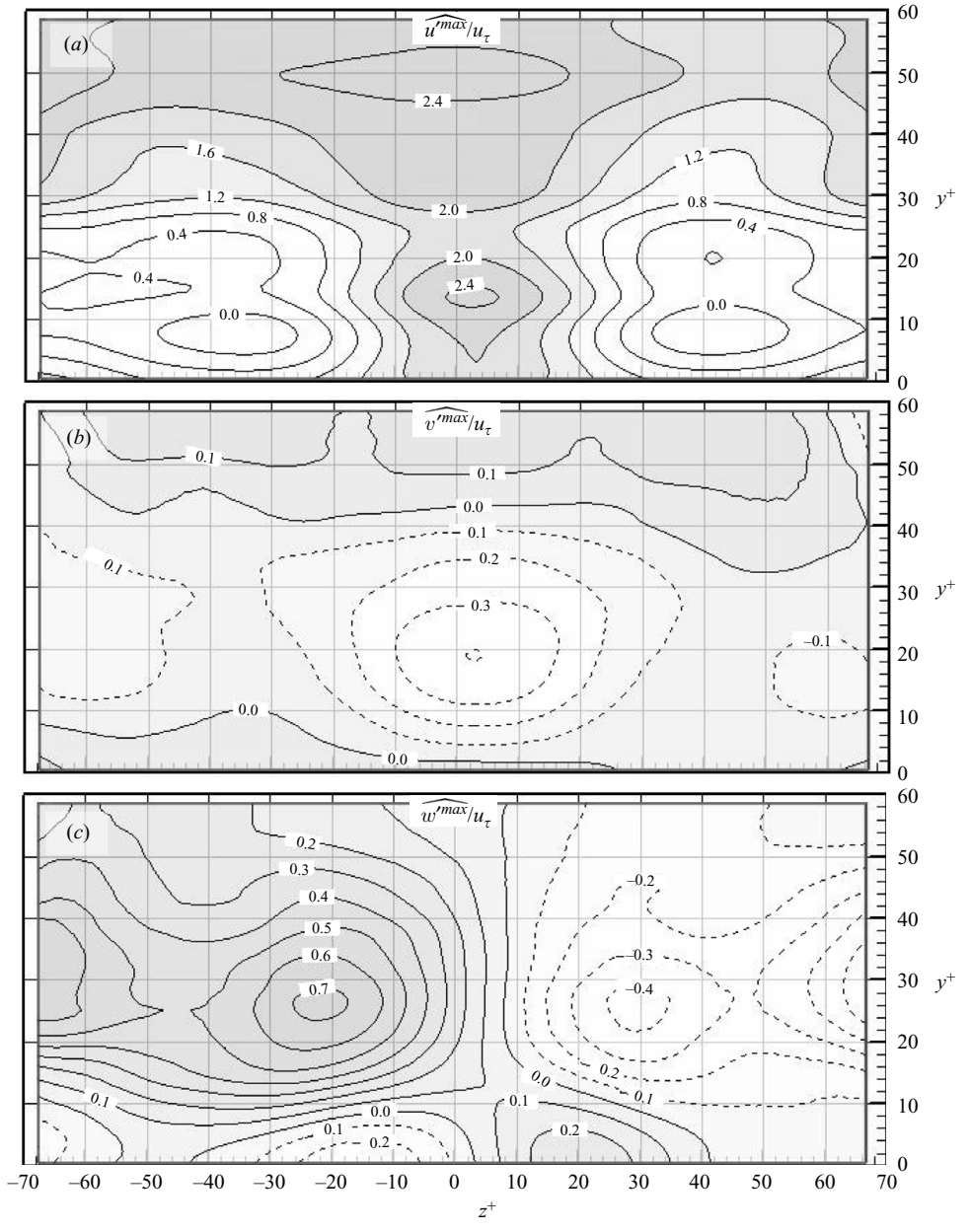

FIGURE 18. A y–z plane at $x^+ = 0$ of conditionally averaged velocity fluctuations based on a local shear maximum for realizations containing single, low-lying vortices without stress minimum upstream (only): (*a*) $\widehat{u'^{max}}/u_\tau$, (*b*) $\widehat{v'^{max}}/u_\tau$ and (*c*) $\widehat{w'^{max}}/u_\tau$. Contour intervals are 0.4, 0.1 and 0.1, respectively.

Unlike the counter-rotating pair, the low-lying vortices seem to be located in regions with $\widehat{u'} > 0$ (figure 18*a*), and vortex-induced entrainment creates a broad region with $\widehat{u'}/u_\tau > 2$ on both sides of the centreline ($z^+ = 0$) that widens with increasing elevation. Outward of the vortices $\widehat{u'}$ drops to nearly 0, presumably due to vortex-induced backward flow, consistent with the orientation of inclined vortex

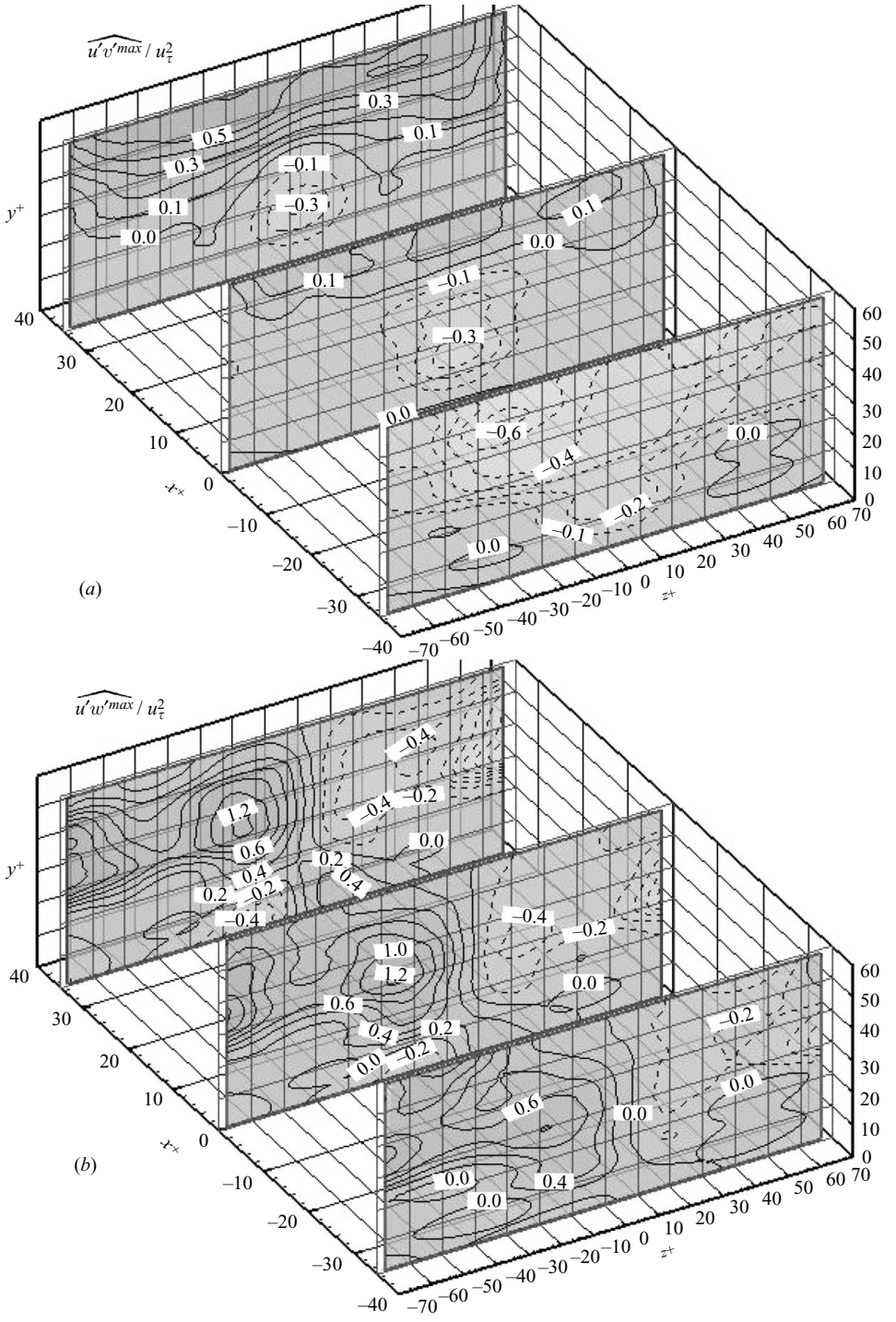

FIGURE 19. Conditionally averaged Reynolds shear stresses based on local shear maximum for realizations containing single, low-lying vortices without stress minimum upstream (only): (*a*) $\widehat{u'v'^{max}}/u_\tau^2$ and (*b*) $\widehat{u'w'^{max}}/u_\tau^2$. Contour intervals are 0.1 and 0.2, respectively. Location of planes is the same as in figure 17.

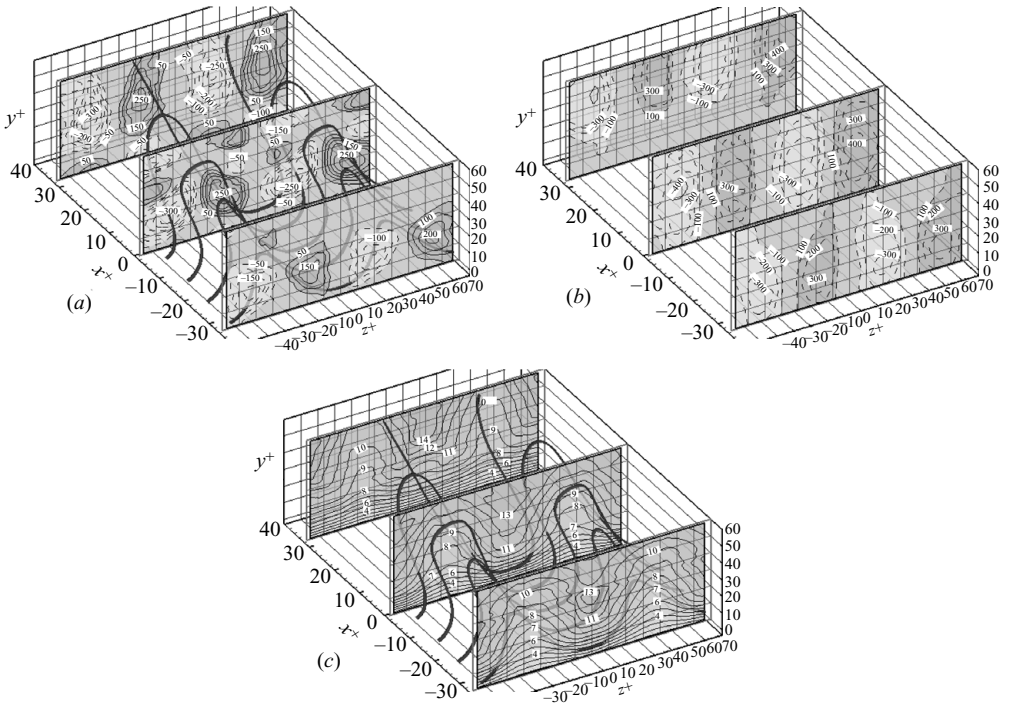

FIGURE 20. Conditionally averaged flow based on local shear maximum for realizations with staggered stress minimum upstream (counter-rotating vortex pair) only: (*a*) $\widehat{\omega_x^{max}}\delta/u_\tau$ and (*b*) $\widehat{\omega_y^{max}}\delta/u_\tau$. Contour intervals are 50 and 100, respectively. (*c*) Mean streamwise velocity component, $\widehat{u^{max}}/u_\tau$. Contour interval is 1.0. Location of planes is the same as in figure 17.

lines. Interestingly, $\widehat{v'}$ is negative below $y^+ = 40$. While a sweeping flow near the centre is expected, one wonders why $\widehat{v'}$ is negative outward of the vortices, where the induced flow should be upward. One speculation could be that the low-lying vortices preferentially exist in a region of downward flow. A second plausible explanation is related to our conditional-averaging procedure. Since we position each single vortex off the centreline in order to locate the wall stress peak at the centre, more area with downflow is inherently included in the averaged distribution, irrespective of the vortex location or direction of rotation. Consequently, our conditional averaging plausibly generates a weak background downflow.

4.3.3. *Sections through vortex pairs generated from lifted spanwise vorticity*

As discussed before, all the samples in this group have a stress minimum upstream of the maximum and involve the same data discussed in §4.2. Consequently, figure 20 presents only distributions of $\widehat{\omega_x}$, $\widehat{\omega_y}$ and $\widehat{u}$ in order to contrast them with results discussed in the previous section. Information on velocity fluctuations and Reynolds stresses is available in figures 13 and 14, but $x^{+max} \approx x^{+min} - 35$ and $z^{+max} \approx z^{+min} \pm 35$. Thus, the plane of minimum wall stress is $x^{+max} = -35$, and and $x^{+max} = 35$ is located $70\delta_\upsilon$ from the minimum. Figure 20(*a*) clearly shows the rapid rise of vortex centre away from the wall, the previously discussed formation of multiple $\widehat{\omega_x}$ peaks in the plane of maximum stress due to backward bending of vortex lines and the disappearance of these multiple peaks as all the vortex lines bend forward at $x^{+max} = 35$. However, this plane contains additional $\widehat{\omega_x}$ peaks in the

viscous sublayer and lower part of the buffer layer due to formation of a spanwise shear layer under the vortices. Figure 20(*c*) shows that the region with streamwise momentum deficit becomes narrower and increases in height with increasing distance from the minimum stress point. As described in § 4.2, narrowing is caused by spanwise entrainment of higher-momentum fluid under the vortices. The vertical extension is caused by self-induced upward flow, which elevates the heads of lifted vortex arches to regions with higher $\widehat{u}$, leading to increased forward stretching. The sample vortex lines clearly demonstrate this rapid stretching process.

5. Summary of observations and comparison to prior studies

In this section, we first summarize the present observations and then compare them with several prominent near-wall structure models found in the literature. Using the first simultaneous measurements of the instantaneous wall shear stress and three-dimensional velocity distribution in the near-wall region, we conditionally sample the three-dimensional velocity, vorticity and stress fields based on extreme events of the local wall stress, i.e. a local stress maximum ($\tau_{xy} > 1.8\langle\tau_{xy}\rangle$) and minimum ($\tau_{xy} < 0.6\langle\tau_{xy}\rangle$). With a reasonably large dataset for conditional sampling, 250 realizations and high spatial resolution, a grid spacing of $1.5 \times 1.2 \times 1.5\delta_\upsilon$ (after interpolations), the conditionally averaged measurement offers a statistically significant, fully spatially resolved view on near-wall flow structures. This process enables us, for the first time, to measure, without any assumptions, relationships among three-dimensional buffer layer structures and the wall shear stress at high Reynolds numbers. Some of the present conclusions are consistent with previously published data and provide experimental confirmations and quantification of trends and impacts. However, some of the observed trends are inconsistent with claims based on analysis of DNS data. In summary, we show that two distinctly different buffer layer flow structures contribute to occurrence of extreme wall stress events.

As illustrated in figure 21, the first structure develops as spanwise vorticity lifts abruptly from the wall, creating initially a vertical arch, which is subsequently stretched both vertically and in the streamwise direction, culminating in formation of a pair of inclined, counter-rotating vortices with ejection (anti-splatting) flow between them. The inclination angle of these vortices is high, well above 45°, based on the orientation of the λ_2 isosurfaces, and above 60°, based on the orientation of the vorticity in the centre of the vortex. Distributions of streamwise velocity explain the spatial variations in the shape of vortex lines during early stages of development. A wall stress minimum exists under the point of initial lifting. A pair of stress maxima develop further ($\sim 35\delta_\upsilon$) downstream during early stages of vortex roll-up, on the outer (downflow) sides of the vortex pair. Consequently, they are displaced laterally by 35–$40\delta_\upsilon$ from the minimum. Associated with this pair of inclined vortices is a complicated, completely three-dimensional distribution of velocity fluctuations and fluxes. For example, near the wall, spanwise transport of streamwise momentum plays a dominant role in formation of the wall stress maxima, and vertical transport is small. In other regions, e.g. during initial lifting, and between the vortices further downstream, vertical transport dominates. This flow structure exists not only in the conditionally averaged field based on stress minimum (figure 7) but in the instantaneous measurement as well (figure 8). Its appearance in 16.4 % of the total realizations (40 cases out of 250) indicates that this structure is statistically significant and plays a major role in near-wall flow dynamics. Since this counter-rotating pair generates two stress maxima,

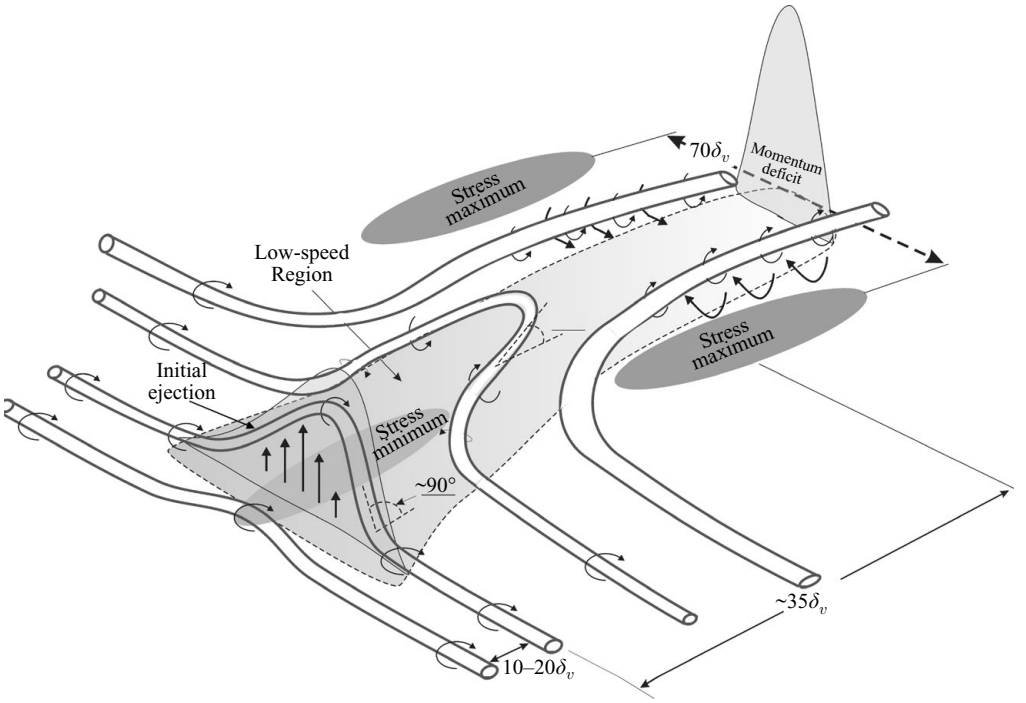

FIGURE 21. A conceptual model illustrating the process of spanwise vortex lifting and the resulting formation of a counter-rotating vortex pair, regions with wall stress extremes and low-momentum region.

conditional sampling based on stress maximum positions vortex pairs on both sides of the maximum. Such a configuration does not exist in instantaneous realizations.

Several features of the structure depicted in figures 7 and 21 agree with those observed qualitatively, deduced from conditional sampling or conjectured in early experimental studies (e.g. Kline *et al.* 1967; Willmarth & Tu 1967; Hinze 1975; Acarlar & Smith 1987; see also Robinson 1991). With some variations, they all describe a phenomenon involving lifting and re-orientation of spanwise vorticity, followed by stretching and formation of an unstable shear layer, culminating in rapid lifting or breakup, i.e. bursting. On one hand, our results provide quantitative details on processes leading to formation of the vortex pair, while on the other hand we highlight several differences. For example, although there are slight bumps in vortex lines well upstream of the minimum wall stress point, the present initial vertical lifting of spanwise vorticity occurs abruptly and within a short distance of about 10 wall units. This predominantly *vertical* lifting, with $|\widehat{u'v'}| > 3u_\tau^2$, is the primary contributor to formation of streamwise momentum deficit and a wall stress minimum. Further downstream, vertical and lateral transport by the vortex-induced motion decreases the width of the low-speed region (perhaps streak) and increases its height. However, the abrupt increase in momentum deficit is clearly caused by the initial lifting. Thus, unlike previous reports, we show that development of a streamwise velocity deficit is not dominated by ejection induced by the counter-rotating pair of streamwise vortices.

As the vortices develop, the strength of ejection between them increases, even creating a region with $|\widehat{u'v'}| > 4.5u_\tau^2$ near the centreline, 60 wall units downstream

of the minimum wall stress point (figure 14). Such trends may lead to a perception of increased instability with streamwise distance. However, the momentum deficit is created earlier. One may question whether the presently observed abrupt lifting and re-orientation of spanwise vorticity is a bursting phenomenon. The order of events is inconsistent with the above-mentioned sequence; i.e. the present violent lifting occurs prior to the formation of a vortex pair. Although we cannot determine the streamwise length of this streak due to the limited size of the sample volume, the flow phenomenon does bear basic features of busting, i.e. abrupt eruption of fluid away from the wall and this eruption leading to formation of a low-speed streak with substantial velocity deficit. Thus, we have most likely captured a high-Reynolds-number bursting process. Since the entire event, from initial lifting to formation of a vortex pair, occurs within a streamwise distance of less than 45 wall units, is it possible that observations based on flow visualization or conditional sampling of point measurements may not be able to distinguish between effects of initial lifting and formation of a pair of vortices? Is the inconsistency related to Reynolds number effects?

We do not know why the initial abrupt lifting occurs; it looks like some kind of instability. Within the range of our measurements, the only precursors are a slight velocity deficit that does not involve an inflection point and relatively low levels of vertical vorticity. Thus, as mentioned before, it is possible that abrupt lifting develops within 'remnants' of a previous low-speed streak, consistent with location of bursting in Jimenez & Pinellli (1999). However, unlike their DNS-based analysis, there is no streamwise vortex or any significant streamwise vorticity upstream of the point of lifting, at least within $y^+ < 88$. Instead, the vortex pair originates from re-oriented spanwise vorticity. Unlike Acarlar & Smith (1987), lack of an inflection point or a substantial momentum deficit in the instantaneous velocity profile upstream of lifting suggests that only a slight deficit may be sufficient for this instability to develop. It is not clear whether it is the same type of instability or whether the present higher Reynolds number requires less deficit to trigger a similar phenomenon.

Induced motion under the rapidly rising vortex pair generates a spanwise shear layer with counter-rotating streamwise vorticity near the wall, leaving clear signatures on the distribution of spanwise wall stress. We cannot at this time follow the development of this 'second generation' of streamwise vorticity and determine whether it results in formation of additional significant streamwise vortices further downstream. (We will do that in future studies.) We also cannot determine whether the counter-rotating pair become legs of or connected in any way with outer layer vortices (Adrian *et al.* 2000; Ganapathisubramani *et al.* 2005; Hutchins *et al.* 2005; Hambleton, Hutchins & Marusic 2006). In only a very few cases, 6 out of 250, which do not satisfy the stress maximum or minimum criteria, we have seen a spanwise linkage of the pair (see § 3.2), i.e. what seems to be a complete hairpin. However, it is likely that our limited measurement volume prevents us from seeing more of them.

As noted before, conditional sampling based on stress minimum shows a distance of $70\delta_\upsilon$ between stress maxima, and sampling based on stress maximum shows a distance of $100\delta_\upsilon$ between stress minima. The corresponding values, if we use δ_υ^R instead, which is based on the peaks in Reynolds stresses, are $84\delta_\upsilon^R$ and $120\delta_\upsilon^R$, respectively, and those based on δ_υ^{CCM}, i.e. the Clauser chart method, are $92\delta_\upsilon^{CCM}$ and $132\delta_\upsilon^{CCM}$, respectively. Thus, the length scales vary depending on the sampling procedure and selected reference length scale. However, results fall within the range of distance between low-speed streaks of about 100 wall units reported in the literature, either based on numerical results (Jimenez & Pinelli 1999) or experimental data (e.g. Willmarth & Lu 1972).

Several publications that are based on analysis of computational data claim that pairs of counter-rotating vortices with similar strength do not play a significant role in buffer layer dynamics (e.g. Kim *et al.* 1971; Jimenez & Pinellli 1999; Schoppa & Hussain 2000, 2002). These conclusions are inconsistent with the present results. Is it a result of differences in conditional sampling criteria, or is it a result of the spatial resolution in the simulations? Daring to raise a question in an area that we know little about, is it possible that the DNS do not sufficiently resolve a phenomenon that develops with little prior warning in about 10 wall units and involves generation of vortices with similar and frequently smaller characteristic size during early stages? The above-mentioned numerical simulations have a wall-normal resolution of less than 1 wall unit but streamwise and spanwise resolutions of 7 and 5 wall units, respectively (Kim *et al.* 1987). Thus, the entire abrupt lifting occurs within one or two streamwise grids of the DNS. Furthermore, the streamwise distance between stress minimum and maximum is five grid points, during which the entire process from initial lifting to formation of a counter-rotating vortex pair occurs. One wonders whether such grid spacing is insufficient for resolving the structures described in most of this paper. As for the significance of these structures, we show that abruptly forming vortex pairs with similar strength developing from lifted and bent spanwise vorticity do exit in statistically significant numbers. Furthermore, they play an important role in generation of extreme wall stress events.

The second structure contributing mostly to high-stress events is a single, predominantly streamwise vortex, which is embedded within the buffer layer. This vortex is larger than those generated by abrupt lifting with characteristic size of 20–40 wall units, and its average inclination angle with the free stream is only 12°. This vortex has been observed in 51 (out of 250) realizations; i.e. it is also statistically significant. By defining it as a single vortex, we do not imply that it is the only structure in the sample volume. In fact, the single vortex often resides with other vortices whose alignments and strengths seem to be random and as a result have little impact on the conditionally averaged flow. This vortex generates an elongated, strong-stress maximum on one side and a weak minimum on the other. Only in one case, the minimum associated with this vortex satisfies the present low-stress criterion. Associated with this vortex is a three-dimensional distribution of velocity fluctuations and fluxes. However, except for a limited region of sweep above the high-stress region, this low-lying vortex mostly induces spanwise momentum transport. In our limited spatial range, we cannot provide meaningful information on how such structures form. Consistent with Kravchenko *et al.* (1993), the single vortex can be located on either side of the point of maximum stress, and as a result, the conditionally averaged flow based on stress maximum shows two counter-rotating structures generating a splatting flow between them.

As summarized in the introduction, existence of slightly inclined, predominantly streamwise vortices in the buffer layer and their important role in formation of low-speed streaks has been reported in many studies based on DNS data (e.g. Kim *et al.* 1987; Jimenez & Pinelli 1999; Schoppa & Hussain 2000). The prevailing view is that stretched quasi-streamwise vortices (Kravchenko *et al.* 1993) or staggered streamwise vortices (Schoppa & Hussain 2000) are responsible for spatial distributions of wall shear stresses and all near-wall dynamics. Thus, it is likely that we are seeing the same (or very similar) phenomenon. There are several similarities. First, the present spacing between (weak-)stress minima on both sides of the conditionally averaged maximum is $\sim 85\delta_\upsilon (101\delta_\upsilon^R, 112\delta_\upsilon^{CCM})$; i.e. lateral scales are consistent with those associated with low-speed streaks in the numerical (and experimental) results. We cannot comment on

the streamwise extent of this structure, since it is undoubtedly influenced by the length of our sample volume. Second, as Jimenez & Pinelli (1999) observed, the low-speed streaks are bounded by regions with substantial wall-normal vorticity, which they find to be convenient for defining the boundaries of the streak. This observation agrees with the present high values of wall-normal vorticity, which exceeds the horizontal component along the vortex centre. Third, although the magnitudes of inclination angles vary, e.g. 10°–12° in Adrian & Moin (1988), 11° in Joeng & Hussain (1995, 1997), 20° in Hutchings *et al.* (2005), they are small, in agreement with the present data. On the other hand, unlike the conclusions of Schoppa & Hussain (2000, 2002), isolated streamwise vortices do not seem to be major contributors to generation of regions with extremely low shear stresses. Finally, we should note that the axial extent of the present data does not allow us to adequately examine interactions among streamwise structures and mechanisms causing them to rise away from the surface. Thus, we cannot comment whether these vortices lift away from the surface periodically (Jimenez & Pinelli 1999) or whether they form staggered streamwise vortices with opposite signs (Schoppa & Hussain 2000). However, as noted before, the low-lying vortices often coexist with other structures and have kinks and extensions, which may be a result of such interactions.

This research was supported in part by the ONR (program manager R. Joslin) under grant N000140310361 and in part by the NSF under grant no. CTS 0625571 (program managers M. Plesniak and W. Schultz). Funding for the optical and computer instrumentation used in this study was provided by the NSF MRI grant CTS0079674. The authors also wish to thank James Wallace for guidance about early studies.

REFERENCES

Acarlar, M. S. & Smith, C. R. 1987 A study of hairpin vortices in a laminar boundary layer. *J. Fluid Mech.* **175**, 1–41.

Adrian, R. J. 1991 Particle-imaging techniques for experimental fluid-mechanics. *Annu. Rev. Fluid Mech.* **23**, 261–304.

Adrian, R. J., Meinhart, C. D. & Tomkins, C. D. 2000 Vortex organization in the outer region of the turbulent boundary layer. *J. Fluid Mech.* **422**, 1–54.

Adrian, R. J. & Moin, P. 1988 Stochastic estimation of organized turbulent structure: homogeneous shear-flow. *J. Fluid Mech.* **190**, 531–559.

Antonia, R. A. 1981 Conditional sampling in turbulence measurement. *Annu. Rev. Fluid Mech.* **13**, 131–156.

Aubry, N., Holmes, P., Lumley, J. L. & Stone, E. 1988 The dynamics of coherent structures in the wall region of a turbulent boundary-layer. *J. Fluid Mech.* **192**, 115–173.

Bakewell, H. P.& Lumley, J. L. 1967 Viscous sublayer and adjacent wall region in turbulent pipe flow. *Phys. Fluids* **10**, 1880–1889.

Bech, K. H., Tillmark, N., Alfredsson, P. H. & Anderson, H. I. 1995 An investigation of turbulent plane Couette flow at low Reynolds number. *J. Fluid Mech.* **286**, 291–325.

Bradshaw, P. & Huang, G. P. 1995 The law of the wall in turbulent flow. *Proc. R. Soc. Lond* A **451**, 165–188.

Clark, J. A. & Markland, E. 1971 Flow visualization in turbulent boundary layer. *J. Hydraul. Div. ASCE* **97**, 1653–1664,

Clauser, F. H. 1956 The turbulent boundary layer. *Adv. Appl. Mech.* **4**, 1–51.

Corino, E. R. & Brodkey, R. S. 1969 A visual investigation of the wall region in turbulent flow. *J. Fluid Mech.* **37**, 1–37.

Djenidi, L. & Antonia, R. A. 1993 LDA measurements in low Reynolds number turbulent boundary layer. *Exp. Fluids* **14**, 280–288.

Ganapathisubramani, B., Hutchins, N., Hambleton, W. T., Longmire, E. K. & Marusic, I. 2005 Investigation of large-scale coherence in a turbulent boundary layer using two-point correlations. *J. Fluid Mech.* **524**, 57–80.

Ganapathisubramani, B., Longmire, E. K. & Marusic, I. 2003 Characteristics of vortex packets in turbulent boundary layers. *J. Fluid Mech.* **478**, 35–46.

George, W. K. & Castillo, L. 1997 Zero-pressure-gradient turbulent boundary layer. *Appl. Mech. Rev.* **50**, 689–729.

Gopalan, S., Abraham, B. M. & Katz, J. 2004 The structure of a jet in cross flow at low velocity ratios. *Phys. Fluids* **16**, 2067–2087.

Hambleton, W. T., Hutchins, N. & Marusic, I. 2006 Simultaneous orthogonal-plane particle image velocimetry measurements in a turbulent boundary layer. *J. Fluid Mech.* **560**, 53–64.

Hamilton, J. M., Kim, J. & Waleffe, F. 1995 Regeneration mechanisms of near-wall turbulence structures. *J. Fluid Mech.* **287**, 317–348.

Hanratty, T. J. 1989 A conceptual model of the viscous wall region. In *Near Wall Turbulence: Proceedings of the Zaric Memorial Conference*, New York (ed. S. J. Kline & N. H. Afghan). pp. 81–103.

Head, M. R. & Bandyopadhyay, P. 1981 New aspects of turbulent boundary-layer structure. *J. Fluid Mech.* **107**, 297–338.

Herzog, S. 1986 The large-scale structure in the near-wall region of turbulent pipe flow. PhD Thesis. Cornell University.

Hinze, J. O. 1975 *Turbulence*. McGraw-Hill.

Holmes, P., Lumley, J. L. & Berkooz, G. 1996 *Turbulence, coherent structures, dynamical systems, and symmetry*. Cambridge University Press.

Hutchins, N., Hambleton, W. T. & Marusic, I. 2005 Inclined cross-stream stereo particle image velocimetry measurements in turbulent boundary layers. *J. Fluid Mech.* **541**, 21–54.

Itano, T. & Toh, S. 2001 The dynamics of bursting process in wall turbulence. *J. Phys. Soc. Jpn* **70**, 701–714.

Itano, T. & Toh, S. 2005 Interaction between large-scale structure and near-wall structures in channel flow. *J. Fluid Mech.* **524**, 249–262.

Jeong, J. & Hussain, F. 1995 On the identification of a vortex. *J. Fluid Mech.* **285**, 69–94.

Jeong, J., Hussain, F., Schoppa, W. & Kim, J. 1997 Coherent structures near the wall in a turbulent channel flow. *J. Fluid Mech.* **332**, 185–214.

Jimenez, J. 1999 The physics of wall turbulence. *Physica* A **263**, 252–262.

Jimenez, J. 2000 Intermittency and cascades. *J. Fluid Mech.* **409**, 99–120.

Jimenez, J., Del Alamo, J. C. & Flores, O. 2004 The large-scale dynamics of near-wall turbulence. *J. Fluid Mech.* **505**, 179–199.

Jimenez, J. & Hoyas, S. 2008 Turbulent fluctuations above the buffer layer of wall bounded flows. *J. Fluid Mech.* **611**, 215–236.

Jimenez, J., Kawahara, G., Simens, M. P., Nagata, M. & Shiba, M. 2005 Characterization of near-wall turbulence in terms of equilibrium and "bursting" solutions. *Phys. Fluids* **17**, (015015)1-16.

Jimenez, J. & Pinelli, A. 1999 The autonomous cycle of near-wall turbulence. *J. Fluid Mech.* **389**, 335–359.

Kasagi, N., Hirata, M. & Nishino, K. 1986 Streamwise pseudo-vortical structures and associated vorticity in the near-wall region of a wall bounded turbulent shear-flow. *Exp. Fluids* **4**, 309–318.

Kawahara, G., Ayukawa, K., Ochi, J. & Ono, F. 1998 Bursting phenomena in a turbulent square-duct flow (generation mechanisms of turbulent wall skin friction). *JSME Intl J.* B **41**, 245–253.

Kawahara, G. & Kida, S. 2001 Periodic motion embedded in plane couette turbulence: regeneration cycle and burst. *J. Fluid Mech.* **449**, 291–300.

Kim, J. 2003 Control of turbulent boundary layers. *Phys. Fluids* **15**, 1093–1105.

Kim, H. T., Kline, S. J. & Reynolds, W. C. 1971 The production of turbulence near a smooth wall in a turbulent boundary layer. *J. Fluid Mech.* **50**, 133–160.

Kim, J., Moin, P. & Moser, R. 1987 Turbulence statistics in fully-developed channel flow at low Reynolds-number. *J. Fluid Mech.* **177**, 133–166.

KLEBANOFF, P. S. 1954 Characteristics of turbulence in a boundary layer with zero pressure gradient. NCAA Report-1247, 1135–1153.

KLEBANOFF, P. S., TRDSTROM, K. D. & SARGENT, L. M. 1962 The three-dimensional nature of boundary-layer instability. *J. Fluid Mech.* **12**, 1.

KLEWICKI, J. C. & HIRSCHI, C. R., 2004 Flow field properties local to near-wall shear layers in a low Reynolds number turbulent boundary layer. *Phys. Fluids*, 4163–4176.

KLINE, S. J., REYNOLDS, W. C., SCHRAUB, F. A. & RUNDSTADLER, P. W. 1967 The structure of turbulent boundary layers. *J. Fluid Mech.* **30**, 741–777.

KOBAYASHI, H. 2008 Large eddy simulation of magnetohydrodynamic turbulent duct flows. *Phy. Fluids* **20**, (015102)1-13.

KRAVCHENKO, A. G., CHOI, H. C. & MOIN, P. 1993 On the relation of near-wall streamwise vortices to wall skin friction in turbulent boundary-layers. *Phys. Fluids* A **5**, 3307–3309.

LIU, Z., ADRIAN, R. J. & HANRATTY, T. J. 2001 Large-scale modes of turbulent channel flow: transport and structure. *J. Fluid Mech.* **448**, 53–80.

LUMLEY, J. L. 1983 Turbulence modeling. *J. Appl. Mech., Trans. ASME* **50**, 1097–1103.

MARUSIC, I. & HEUER, W. D. C. 2007 Reynolds number invariance of the structure inclination angle in wall turbulence. *Phys. Rev. Lett.* **99**.

NAKAGAWA, H. & NEZU, I. 1981 Structure of space-time correlations of bursting phenomena in an open-channel flow. *J. Fluid Mech.* **104**, 1–43.

NIEDERSCHULTE, M. A., ADRIAN, R. J. & HANRATTY, T. J. 1990 Measurements of turbulent flow in a channel at low reynolds numbers. *Exp. Fluids* **9**, 222–230.

OFFEN, G. R. & KLINE, S. J. 1975 Proposed model of bursting process in turbulent boundary-layers. *J. Fluid Mech.* **70**, 209–228.

OFTEN, G. R. & KLINE, S. J. 1974 Combined dye-streak and hydrogen-bubble visual observations of a turbulent boundary layer. *J. Fluid Mech.* **62**, 223–239.

PERRY, A. E. & CHONG, M. S. 1982 On the mechanism of wall turbulence. *J. Fluid Mech.* **119**, 173–217.

PERRY, A. E. & CHONG, M. S. 1986 A series-expansion study of the Navier–Stokes equations with applications to 3-dimensional separation patterns. *J. Fluid Mech.* **173**, 207–223.

PERRY, A. E., HENBEST, S. & CHONG, M. S. 1986 A theoretical and experimental-study of wall turbulence. *J. Fluid Mech.* **165**, 163–199.

POPE, S. B. 2000 *Turbulent Flow*. Cambridge University Press.

PRATURI, A. K. & BRODKEY, R. S. 1978 Stereoscopic visual study of coherent structures in turbulent shear-flow. *J. Fluid Mech.* **89**, 251–272.

ROBINSON, S. K. 1991 Coherent motions in the turbulent boundary-layer. *Annu. Rev. Fluid Mech.* **23**, 601–639.

SCHOPPA, W. & HUSSAIN, F. 2000 Coherent structure dynamics in near-wall turbulence. *Fluid Dyn. Res.* **26**, 119–139.

SCHOPPA, W. & HUSSAIN, F. 2002 Coherent structure generation in near-wall turbulence. *J. Fluid Mech.* **453**, 57–108.

SHENG, J., MALKIEL, E. & KATZ, J. 2003 Single beam two-views holographic particle image velocimetry. *Appl. Optics* **42**, 235–250.

SHENG, J., MALKIEL, E. & KATZ, J. 2006 Digital holographic microscope for measuring three-dimensional particle distributions and motions. *Appl. Optics* **45**, 3893–3901.

SHENG, J., MALKIEL, E. & KATZ, J. 2008 Using digital holographic microscopy for simultaneous measurements of 3d near wall velocity and wall shear stress in a turbulent boundary layer. *Exp. Fluids* **45**, 1023–1035.

SHENG, J., MALKIEL, E., KATZ, J., ADOLF, J., BELAS, R. & PLACE, A. R. 2007*a* Digital holographic microscopy reveals prey-induced changes in swimming behavior of predatory dinoflagellates. *Proc. Nat. Acad. Sci. USA* **104**, 17512–17517.

SHENG, J., MALKIEL, E., KATZ, J., ADOLF, J. E., BELAS, R. & PLACE, A. R. 2007*b* Prey-induced changes in swimming behavior of predatory dinoflagellates. *J. Phycol.* **43**, 25–25.

SMITH, C. R. 1984 A synthesized model of the near-wall behavior in turbulent boundary layers. *Symp. Turbul., 8th.*

SMITH, C. R. & LU, L. J. 1989 The use of a template-matching technique to identify hairpin vortex flow structures in turbulent boundary layers. In *Near Wall Turbulence: Proceedings of the Zaric Memorial Conference*, New York (ed. S. J. Kline & N. H. Afgan) pp. 248–267.

Smith, C. R. & Metzler, S. P. 1983 The study of hairpin vortices in a laminar boundary layer. *J. Fluid Mech.* **129**, 27–54.

Smith, C. R. & Schwartz, S. P. 1983 Observation of streamwise rotation in the near wall region of a turbulent boundary layer. *Phys. Fluids* **26**, 241–252.

Suponitsky, V., Cohen, J. & Bar-yoseph, P. Z. 2005 The generation of streaks and hairpin vortices from a localized vortex disturbance embedded in unbounded uniform shear flow. *J. Fluid Mech.* **535**, 65–100.

Tao, B., Katz, J. & Meneveau, C. 2000 Geometry and scale relationships in high reynolds number turbulence determined from three-dimensional holographic velocimetry. *Physics of Fluids* **12**, 941–944.

Tao, B., Katz, J. & Meneveau, C. 2002 Statistical geometry of subgrid-scale stresses determined from holographic particle image velocimetry measurements. *J. Fluid Mech.* **457**, 35–78.

Tennekes, H. & Lumley, J. L. 1972 *A First Course in Turbulence*. MIT Press.

Theodorsen, T. 1952 Mechanism of turbulence. In *Midwest Conference on Fluid Mechanics, Second*, 1–18.

Viswanath, D. 2007 Recurrent motions within plane Couette turbulence. *J. Fluid Mech.* **580**, 339–358.

Waleffe, F. & Kim, J. 1997 *How streamwise rolls and streaks self-sustain in a shear flow self-sustaining mechanisms of wall turbulence. Series: Advances in Fluid Mechanics*, pp. 309–332. MIT Press.

Walker, J. D. A. & Herzog, S. 1988 Eruption mechanisms for turbulent flows near walls. In *Transport Phenomena in Turbulent Flows* (ed. M. Hirata & N. Kasagi), pp. 145–156. Hemisphere.

Wallace, J. 1982 On the structure of bounded turbulent shear flow: a personal view. In *Developments in Theoretical and Applied Mechanics XI* (ed. T. J. Chung), pp. 509–521.

Wallace, J. M., Eckelmann, H. & Brodkey, R. S. 1972 The wall region in turbulent shear flow. *J. Fluid Mech.* **54**, 39–48.

Wei, T., Schmidt, R. & McMurtry, P. 2005 Comment on the clauser chart method for determining the friction velocity. *Exp. Fluids* **38**.

Willmarth, W. W. & Lu, S. S. 1972 Structure of the Reynolds stress near the wall. *J. Fluid Mech.* **55**, 65–92.

Willmarth, W. W. & Tu, B. J. 1967 Structure of turbulence in the boundary layer near the wall. *Phys. Fluids* **10**, S134–137.

Willmarth, W. W. & Woolridge, C. E. 1962 Measurements of the fluctuating pressure at the wall beneath a thick turbulent boundary layer. *J. Fluid Mech.* **14**, 187–210.

Wu, Y. & Christensen, K. T. 2006 Population trends of spanwise vortices in wall turbulence. *J. Fluid Mech.* **568**, 55–76.

Zhang, J., Tao, B. & Katz, J. 1997 Turbulent flow measurement in a square duct with hybrid holographic PIV. *Exp. Fluids* **23**, 373–381.

Zhou, J., Adrian, R. J., Balachandar, S. & Kendall, T. M. 1999 Mechanisms for generating coherent packets of hairpin vortices in channel flow. *J. Fluid Mech.* **387**, 353–396.